MSDE

ROYAL SOCIETY OF CHEMISTRY

REVIEW

Cite this: *Mol. Syst. Des. Eng.*, 2021, **6**, 250

Plasmon-driven photocatalytic molecular transformations on metallic nanostructure surfaces: mechanistic insights gained from plasmon-enhanced Raman spectroscopy

Kexun Chen and Hui Wang *

Optically excited plasmonic nanostructures exhibit unique capabilities to catalyze interfacial chemical transformations of molecules adsorbed on their surfaces in a regioselective manner through anomalous reaction pathways that are inaccessible under thermal conditions. The mechanistic complexity of plasmon-driven photocatalysis is intimately tied to a series of photophysical and photochemical processes associated with the radiative and non-radiative decay of localized plasmon resonances in metallic nanostructures. Plasmon-enhanced Raman spectroscopy combines ultrahigh detection sensitivity with unique time-resolving and molecular finger-printing capabilities, ideal for detailed kinetic and mechanistic studies of photocatalytic interfacial transformations of molecular adsorbates residing in the plasmonic hot spots. Through systematic case studies of several representative reactions, we demonstrate how plasmon-enhanced Raman spectroscopy can be judiciously utilized as a unique *in situ* spectroscopic tool to fine-resolve the detailed molecule-transforming processes on the surfaces of optically excited plasmonic nanostructures in real time during the photocatalytic reactions. We further epitomize the mechanistic insights gained from *in situ* plasmon-enhanced Raman spectroscopic measurements into several central materials design principles that can be employed to guide the rational optimization of the photocatalyst structures and the nanostructure-molecule interfaces for plasmon-mediated surface chemistry.

Received 1st March 2021,
Accepted 11th March 2021

DOI: 10.1039/d1me00016k

rsc.li/molecular-engineering

Design, System, Application

This review article elaborates on important insights extracted from the results of *in situ* plasmon-enhanced Raman spectroscopic measurements, which shed light on the complex mechanisms underpinning the plasmon-driven photocatalytic transformations of molecular adsorbates on nanostructured metal surfaces. These thought-provoking mechanistic insights form a solid knowledge foundation that markedly enhances our capabilities of using plasmon-driven photocatalysis as a deliberately designed, light-triggered tool to precisely tailor the surface molecular moieties and rationally optimize the surface functionalities of metallic nanostructures for specifically targeted applications.

1. Introduction

Virtually all chemically synthesized inorganic nanoparticles are capped with organic molecular ligands on their outer surfaces. The surface-capping molecular ligands may not only significantly modify the intrinsic properties of the nanocrystal cores, but also dynamically modulate the molecular recognition, energy exchange, and charge transfer events occurring between the colloidal nanostructures and their local environment.[1–10] On the other hand, the surface atomic configurations and local surface curvature of the nanoparticles also profoundly influence the architectural arrangements and chemical properties of the organic ligand molecules.[11–16] Therefore, the inorganic nanocrystal cores and the organic ligand shells are two structurally distinct but strongly interplaying components that synergistically determine the collective optical, electronic, and catalytic properties of the nanoparticles. Detailed understanding of the rich chemistry associated with the molecular adsorbates on nanostructured surfaces is of pivotal importance to the selective implementation of desired surface architectures and functionalities in nanoparticle systems for specifically targeted applications in optoelectronics, microscopic imaging, molecular sensing, biomedicine, and heterogeneous catalysis.[1,9,17–19]

Metallic nanostructures represent a unique materials system whose surface properties can be fine-tailored regioselectively through plasmon-mediated interfacial molecule-transforming processes.[20–22] The fascinating tunable optical properties of metallic nanoparticles

Department of Chemistry and Biochemistry, University of South Carolina, Columbia, South Carolina 29208, USA. E-mail: wang344@mailbox.sc.edu; Fax: +1 803 777 9521; Tel: +1 803 777 2203

essentially originate from the collective oscillations of free electrons in the metals, also known as plasmons, localized within the confinement by the nanostructures. Optical excitations of the localized plasmon resonances supported by metallic nanoparticles give rise to a series of intriguing photophysical and photochemical effects, such as enhanced light absorption or scattering at the resonant frequencies, drastically amplified electromagnetic field intensities on the nanoparticle surfaces, localized photothermal heat generation, and creation of transient, energetic hot electrons and holes that are far from the thermal equilibrium.[23–31] These plasmon-derived effects can be judiciously harnessed to effectively drive or catalyze interfacial molecular transformations on nanoparticle surfaces through anomalous reaction pathways strikingly distinct from those typically involved in thermally activated heterogeneous catalysis and the exciton-driven photocatalysis on semiconductors.[31–34] While a diverse set of plasmon-driven photocatalytic reactions have been discovered in succession over the past decade,[20–22,31–42] many aspects concerning the detailed reaction mechanisms still remain elusive and open to further investigations. Mechanistic insights on the plasmon-mediated interfacial molecular transformations provide key guiding principles one should follow when employing plasmon-driven photocatalysis as a versatile, paradigm-shifting approach to deliberately tailor the surface functionalities of metallic nanostructures.

Besides their roles as plasmonic photocatalysts, optically excited metallic nanoparticles may also function as light-concentrating nanoantennas, creating localized electromagnetic "hot spots", where the field intensities can be enormously enhanced by several orders of magnitude, in the vicinity of their surfaces.[27,29] Such local field enhancements can be exploited to drastically amplify the Raman spectroscopic signals of molecular adsorbates on nanostructured metal surfaces, an interesting phenomenon known as surface-enhanced Raman scattering (SERS).[43–53] In addition to the electromagnetic enhancement, charge transfer between strongly coupled nanostructures and molecular adsorbates can provide additional contribution to the overall enhancement of Raman signals, an effect termed as the chemical enhancement by the SERS community.[52,54–56] SERS has been demonstrated to be an ultrasensitive surface spectroscopic tool for molecular sensing and characterizations, even approaching single-molecule detection sensitivity for certain nanostructure-molecule systems.[47,57–62] In addition, SERS is a vibrational spectroscopy capable of providing detailed molecular fingerprinting information, ideal for thorough structural characterizations of monolayer and sub-monolayer ligand molecules on plasmonic nanostructure surfaces.[28,48,49,63] Furthermore, unlike many other surface characterization techniques, such as electron energy loss spectroscopy (EELS) and X-ray photoelectron spectroscopy (XPS), which require high vacuum environment for spectral acquisition, SERS can be used as an *in situ* spectroscopic tool to monitor the interfacial molecular transformations in real time without separating the nanoparticles from their native environment under reaction conditions.[64–66] Combining its unique structure- and time-resolving capabilities with its superior surface sensitivity, SERS has become an extremely powerful spectroscopic tool for detailed investigations of dynamic ligand exchange and catalytic molecular transformations on nanostructured metal surfaces.[14,16,66–81]

Kexun Chen

Kexun Chen received his B.S. degree in Chemistry from East China University of Science and Technology in 2016 and his M. S. degree in Polymer Science from University of Akron in 2018, respectively. He is currently a Ph.D. candidate working on plasmon-mediated surface chemistry under the supervision of Hui Wang at the University of South Carolina.

Hui Wang

Hui Wang received his B.S. degree in Chemistry with honors from Nanjing University in 2001. He earned his Ph.D. degree in Physical Chemistry from Rice University in 2007 based upon his graduate work on nanoplasmonics conducted under the supervision by Naomi J. Halas. As a postdoctoral research fellow, he worked on single-molecule spectroscopy and biophysics under the tutelage of Paul F. Barbara at the University of Texas at Austin. In 2010, he joined the Department of Chemistry and Biochemistry at the University of South Carolina as a tenure-track Assistant Professor and was promoted to Associate Professor with tenure in 2016. His current research focuses on the optical, catalytic, and photocatalytic properties of complex nanostructures and the mechanisms of interfacial molecular transformations on nanostructured surfaces.

This review article epitomizes important mechanistic insights on plasmon-mediated surface chemistry gained from plasmon-enhanced Raman spectroscopy, including both SERS and tip-enhanced Raman spectroscopy (TERS), over the past ten years or so. We first briefly discuss several key photophysical and photochemical effects derived from the decay of localized plasmon resonances, all of which may play crucial roles in plasmon-mediated molecular transformations. We then elaborate on the detailed mechanisms of several representative types of mechanistically complex plasmon-driven reactions, including both bond-forming coupling reactions and bond-breaking molecular fragmentation. In these studies, the metallic nanostructures play a unique dual-role as both the plasmonic photocatalysts and the substrates for plasmon-enhanced Raman spectroscopy. Through deliberately selected case studies, we demonstrate how detailed structural and kinetic information can be extracted from the *in situ* plasmon-enhanced Raman spectroscopic results to fully unravel the effects of plasmonic hot carriers, photothermal heating, and local field enhancements on the photocatalytic molecular transformations. Next, we further elucidate the mechanisms underpinning plasmon-mediated surface chemistry in a much broader context by highlighting the surprisingly remarkable analogies between plasmon-driven photocatalysis and X-ray or electron beam-induced surface chemistry in terms of the reaction outcomes, despite the fact that the energies of the X-ray photons and electrons incident on the samples are typically more than 100 times higher than those of the light sources utilized for plasmon excitations. Finally, we briefly summarize several key materials design principles distilled from the results of *in situ* SERS and TERS measurements, which provide important guidance to the rational optimization of the nanostructure-adsorbate systems for plasmon-mediated surface chemistry.

2. Plasmon decay pathways and plasmon-mediated surface chemistry

Localized plasmons in metallic nanostructures can be optically excited when the frequency of the incident photons matches the oscillation frequency of the conduction band electrons. Under resonant excitation conditions, the incident electromagnetic waves coherently drive the collective oscillations of free electrons in the conduction band against the restoring force exerted by the positively charged metal nuclei (see the schematic illustration in Fig. 1A). A plasmonically excited metallic nanoparticle behaves as a nanoscale optical antenna that effectively concentrates light within ultrasmall volumes below the diffraction limit of light in close proximity to the nanoparticle surfaces, giving rise to a series of intriguing photophysical and photochemical phenomena that are unobservable in either bulk materials or individual atoms. The plasmonic electron oscillations are short lived with lifetimes typically in the range of 5–100 fs, decaying radiatively through elastic photon scattering and non-radiatively through either Landau damping or chemical interface damping (CID),[34] as schematically illustrated in Fig. 1B.

The radiative decay of plasmons results in large field enhancements of the scattering photons at the nanoparticle surfaces, exploitable not only for plasmon-enhanced spectroscopies but also for plasmon-enhanced intramolecular excitations,[82] which involve the electronic transitions from the highest occupied molecular orbital (HOMO) to the lowest unoccupied molecular orbital (LUMO) of the adsorbates residing in the plasmonic hot spots (Fig. 1C). The rate and efficiency of the intramolecular electronic transitions can be drastically enhanced by the intense scattering photons reradiated from the plasmonic nanoantennas when the energy gap between the HOMO and LUMO matches the energy of the plasmon resonances. In the process of bond cleavage, molecules

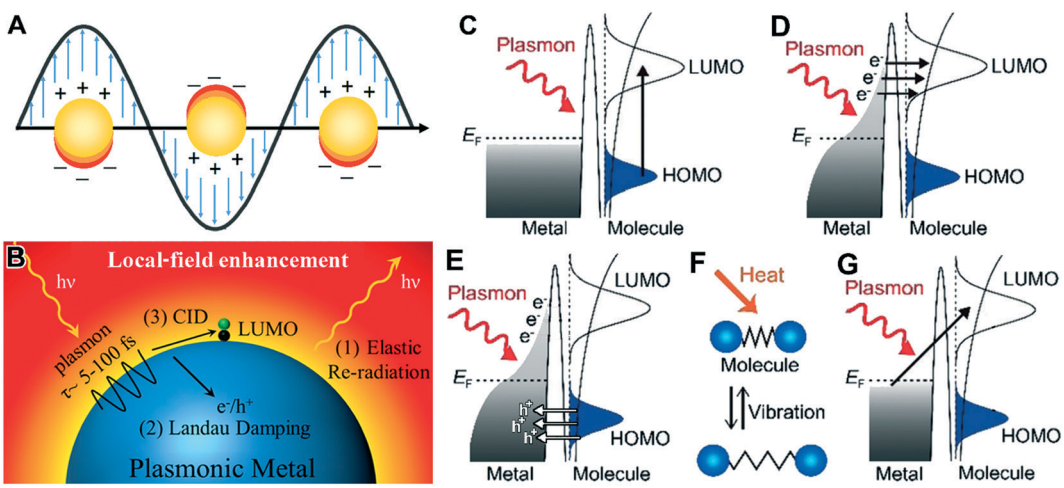

Fig. 1 Schematic illustration of (A) plasmonic electron oscillations in a metal nanoparticle and (B) plasmon decay pathways. Reprinted with permission from ref. 34. Copyright 2014, American Chemical Society. Several mechanisms involved in the plasmon-mediated photocatalysis: (C) plasmon-enhanced intramolecular electronic excitation; (D) indirect hot electron transfer following Landau damping; (E) indirect hot hole transfer following Landau damping; (F) photothermal heating; (G) direct hot electron injection in molecular adsorbates through CID. Reprinted with permission from ref. 82. Copyright 2019, John Wiley and Sons.

in their excited electronic states may either evolve along the potential energy surface of the excited state or relax back to the ground electronic state with additional vibrational energy. In both cases, the activation energy barriers for bond cleavage become significantly lower than in the ground electronic states, an effect that can be interpreted in the context of the Franck–Condon principle.[22,36] Interestingly, the coupling between the molecular adsorbates and the metal surfaces can cause energy shift of the electronic orbitals of the molecules, resulting in reaction energy landscapes different from those of the reactions occurring in aqueous solutions or in the gas phase.[82]

In contrast to the radiative decay, the non-radiative decay of plasmonic electron oscillations serves as the primary channel for generation of photo-excited charge carriers exploitable for photocatalysis.[31–33,83,84] Through non-radiative Landau damping, which typically occurs within ~10 fs after initial plasmon excitation, the energy of absorbed photons is harnessed to excite electron–hole pairs in the metallic nanostructures, giving rise to transient, non-thermal distribution of electrons and holes above and below the Fermi level of the metal, respectively. These photo-excited plasmonic charge carriers are termed as "hot" carriers because they are highly energetic and deviate significantly from the thermal Fermi–Dirac distribution. Unlike excitons in semiconductors, plasmonic hot electrons and hot holes are not intrinsically correlated, undergoing a carrier relaxation process over time-scales ranging from ~100 fs to ~1 ps through inelastic electron–electron scattering rather than electron–hole recombination.[31–33] Through the cascading electron–electron scattering process, the energies of the primary hot electrons are distributed among an increasing number of electrons in the metallic nanostructures, causing the energy distribution of the hot electrons to evolve over time. The resulting lower-energy electrons can couple with the phonon modes to undergo thermal relaxation over the time-scales of ~100 ps to ~10 ns, which leads to local heating at the nanoparticle surfaces followed by heat dissipation to the surrounding media, a process referred to as plasmonic photothermal heating.[31,82] Before becoming fully thermalized, the hot electrons created through Landau damping can be transferred from the metal nanoparticles to the LUMO of the molecular adsorbates to catalyze intriguing interfacial molecular transformations (Fig. 1D). Similarly, the electrons populated in the HOMO of the molecular adsorbates can also be transferred to the metallic nanostructures to trigger hot hole-driven reactions (Fig. 1E). Some hot carrier-driven photocatalytic reactions can be further kinetically boosted due to the elevated temperature at the nanoparticle surfaces under photo-illumination as additional thermal energy is deposited into the molecular vibrations (Fig. 1F). The effects of both plasmonic hot carriers and photothermal heating should be carefully considered and quantitatively evaluated when interpreting the mechanisms of plasmon-driven photocatalytic reactions. Recent studies involving more careful temperature measurements and modeling suggested that the thermal effects on plasmon-driven photocatalysis might have been either overlooked or underestimated in numerous cases,[85–90] and it appeared inappropriate to interpret the origin of the kinetic enhancement solely in the context of plasmonic non-thermal effects for a variety of plasmon-driven reactions.[88–96] These new findings suggest the need to revisit and further scrutinize some conclusions drawn from previous studies[35,39,97] concerning the relative contributions of hot carriers *vs.* photothermal heating to the overall reaction kinetics.

The plasmons in strongly coupled nanoparticle-adsorbate or heteronanostructure systems may decay through an alternative non-radiative pathway known as CID, which involves the direct excitations of electrons in the unpopulated orbitals of molecules or materials that are in contact with the metal nanostructures (Fig. 1G).[34,98,99] The carrier relaxation occurs immediately following Landau damping, which leads to a majority of the hot carriers distributed fairly close to the Fermi level of the metals. Therefore, the electrons generated through Landau damping are more likely to be injected into the adsorbate orbitals whose energies are well-aligned with the Fermi level of the metal. In contrast to Landau damping, CID provides a unique pathway to directly inject electrons into a particular unoccupied orbital of the adsorbates, and is thus considered as a potentially more efficient charge-transfer channel than the indirect charge transfer following the Landau damping. The direct charge excitation through CID results in resonantly excited electrons in an adsorbate orbital of specific energy, offering unique opportunities to kinetically boost specifically targeted electronic transitions and thereby selectively activating molecular transformations associated with those specific transitions. Although the hot carriers derived from Landau damping and CID may exhibit different catalytic efficiencies, reaction selectivity, and energy landscapes, the experimental procedures capable of indisputably distinguishing Landau damping and CID are still essentially non-existent at the current stage.

While the charge transfer from the plasmons to the adsorbates has been the most widely suggested mechanism for CID, the more broadly defined concept of CID also includes other plasmon damping processes caused by the molecular adsorbates. For example, Link and coworkers[100] found that surface adsorbates could induce electric dipoles inside the metal, which acted as additional scattering centers for plasmon dephasing. Plasmon damping may also occur through energy transfer between the metallic nanoparticles and the molecular adsorbates, which becomes most efficient when the absorption band of adsorbates overlaps with the plasmon resonance of the nanoparticles.[101,102] In this context, the plasmon-enhanced intramolecular excitations can also be considered as a pathway of CID.

3. Mechanisms of plasmon-driven photocatalysis: what have we learned from case studies?

The mechanistic complexity of plasmon-mediated surface chemistry can be fully manifested by several examples

discussed in this review article. Some plasmon-driven photocatalytic molecule-transforming processes are synergistically dictated by multiple interplaying plasmon-derived effects rather than being dominated exclusively by one specific plasmon decay mechanism. For certain nanostructure-adsorbate systems, the dominant reaction pathways may even inter-switch among multiple plasmon-decaying channels upon variation of the nanocatalyst structures and detailed reaction conditions, as exemplified by the plasmon-driven nitroaromatics reduction and methylene blue fragmentation reactions, which will be discussed in detail in this review article. Here we discuss the complex mechanisms underpinning plasmon-driven photocatalysis through systematic case studies carried out on several representative reactions, emphasizing on how the contributions of multiple intertwining plasmonic effects can be delineated by scrutinizing the detailed structural and kinetic information extracted from *in situ* SERS and TERS results.

3.1 Plasmon-driven oxidation of *para*-aminothiophenol (*p*ATP)

Formation of 4,4′-dimercaptoazobenzene (DMAB) through plasmon-driven oxidative coupling of surface-adsorbed *p*ATP provides a unique photocatalytic approach to the synthesis of azo compounds on nanostructured surfaces. This plasmon-driven reaction was discovered in 2010 when Tian and coworkers[103] carefully reexamined the origin of several peculiar Raman peaks that were completely absent in the normal Raman spectra but became extraordinarily strong in the SERS spectra of *p*ATP. The discovery of this reaction has been regarded as a milestone in the field of plasmon-driven photocatalysis. First, it has clarified a long-standing controversial issue concerning the correct interpretation of the SERS spectral features of *p*ATP.[103,104] Second, the structural evolution of molecules during this reaction can be fine-resolved at an unprecedented level of precision and detail through *in situ* plasmon-enhanced Raman spectroscopic measurements.[104–106] Third, the oxidative coupling of *p*ATP may occur selectively along a hot electron-driven or a hot hole-driven reaction pathway, depending on the structures of the plasmonic photocatalysts and the detailed conditions under which the reaction occurs.[107] Therefore, the plasmon-driven oxidation of *p*ATP chemisorbed on metallic nanostructure surfaces has become a model reaction ideal for developing detailed mechanistic understanding of plasmon-driven photocatalysis.

*p*ATP has been widely used as a model molecular probe for assessment of SERS activity and construction of SERS tags because of its strong binding affinity to the metal surfaces, known molecular packing density in self-assembled monolayers (SAMs), and well-defined vibrational modes in Raman spectra. However, remarkable discrepancy exists between the normal Raman and SERS spectral features of *p*ATP, which was first identified by Osawa and coworkers in 1994.[108] When measuring the SERS of *p*ATP molecules chemisorbed on surface-roughened Ag substrates, they observed the emergence of three anomalous Raman peaks at 1140, 1388, and 1438 cm^{-1}, which were initially assigned to the vibrational modes of *p*ATP with the b_2 symmetry resulting from charge transfer-induced chemical enhancement.[108] However, Fujishima and coworkers[109,110] argued that the discrepancy between the normal Raman and SERS spectra of *p*ATP could be alternatively interpreted as a result of the production of an azobenzene molecule through *p*ATP dimerization on Ag surfaces. The spectral assignment of the abnormal SERS peaks of *p*ATP had been a controversial topic under intense debate for more than a decade until 2010 when Tian and coworkers convincingly proved that *p*ATP molecules adsorbed on nanostructured Ag surfaces underwent a plasmon-driven photocatalytic coupling reaction to form DMAB under standard conditions for SERS measurements.[103] As shown in Fig. 2A, the SERS peaks originally assigned to the b_2 modes of *p*ATP were actually the characteristic a_g modes of an aromatic azo compound, DMAB. A piece of direct evidence for the formation of DMAB was that the SERS spectral features of chemically synthesized DMAB were in excellent agreement with those of the photo-illuminated *p*ATP adsorbed on roughened Ag electrode surfaces (Fig. 2B). The formation of DMAB was further verified by surface mass spectrometry and potential-dependent SERS. The characteristic peaks of DMAB emerged in the SERS spectra only when the excitation laser power exceeded a certain threshold value, whereas in the low excitation power range, both the normal Raman and SERS spectra exhibited essentially the same set of peaks all belonging to *p*ATP. The plasmon-driven oxidative coupling of *p*ATP occurred not only on roughened Ag electrodes, but also on the surfaces of a large variety of metallic nanostructures, such as individual nanoparticles,[111] colloidal sols,[112,113] nanoparticle aggregates,[114] and nanoparticle-film junctions.[115,116] The spectral assignments of all the characteristic Raman peaks of DMAB were further supported by density functional theory (DFT) calculations.[112,117] Another piece of strong evidence for the production of DMAB through photocatalytic *p*ATP coupling was obtained from time-resolved SERS measurements. The auto-correlation functions for the SERS intensity fluctuations of the a_1 modes of *p*ATP and the a_g modes of DMAB exhibited remarkably different decay behaviors, indicating significant difference in the temporal evolution of *p*ATP and DMAB.[118] The results of scanning confocal Raman microscopy imaging clearly revealed non-identical spatial distribution of *p*ATP and DMAB on the plasmonic photocatalyst surfaces, further verifying the coexistence of both molecular species during the reactions.[118] The plasmon-driven oxidative coupling of *p*ATP provides a prototypical example convincingly demonstrating that unconventional photocatalytic molecular transformations may occur on the surfaces of optically excited metallic nanostructures during SERS measurements. Therefore, SERS should not always be simply considered as a non-invasive spectroscopic tool when characterizing the structures of surface-adsorbed molecules.

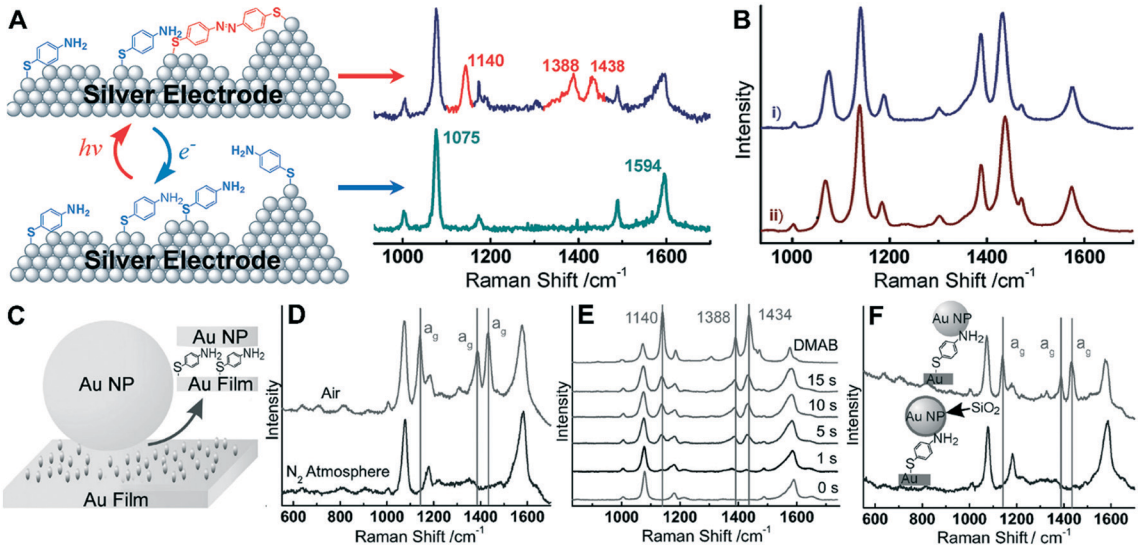

Fig. 2 (A) Schematic illustration of plasmon-driven oxidative coupling of *p*ATP into DMAB on a roughened Ag electrode and the corresponding SERS spectra of *p*ATP before and after photo-illumination. The Raman peaks highlighted in red at 1140, 1388, and 1438 cm^{-1} are assigned to the a_g modes of DMAB. (B) SERS spectra of (i) *p*ATP and (ii) pre-synthetized DMAB on roughened Ag electrodes excited by a 632.8 nm laser at a power density of ~100 kW cm^{-2}. Reprinted with permission from ref. 103. Copyright 2010, American Chemical Society. (C) Schematic illustration of a *p*ATP monolayer sandwiched between an Au film and an Au nanoparticle, denoted as Au/*p*ATP/Au NP. (D) SERS spectra of Au/*p*ATP/Au NPs recorded in air and in an N_2 atmosphere. (E) Temporal evolution of SERS spectra collected on Au/*p*ATP/Au NPs during plasmon-driven coupling of *p*ATP in air. (F) SERS spectra collected on Au/*p*ATP/Au NP and Au/*p*ATP/Au@SiO_2 NP junctions in air. Reprinted with permission from ref. 115. Copyright 2014, John Wiley and Sons.

The kinetics of plasmon-driven oxidative coupling of *p*ATP was observed to be sensitively dependent upon the atmospheres in which the reaction took place. For example, *p*ATP molecules sandwiched between an Au nanoparticle (Au NP) and an Au film (see schematic illustration in Fig. 2C) underwent rapid coupling reactions to produce DMAB in ambient air during SERS measurements, whereas no DMAB was produced in an N_2 atmosphere (Fig. 2D).[115] This observation suggested that one or more components in air played crucial roles in triggering this reaction. The reaction progress could be monitored in real time through time-resolved SERS measurements (Fig. 2E). At the initial stage of the reaction, the SERS spectral features were dominated by two Raman peaks at 1078 and 1595 cm^{-1}, which could be assigned to the C–S bond stretching and the benzene ring mode of *p*ATP, respectively. As the reaction proceeded, the signature peaks of DMAB located at 1140, 1388, and 1438 cm^{-1} became progressively more intense. It has been reported that photoexcited hot electrons in Au and Ag nanoparticles can transfer to the antibonding $2\pi^*$ orbital of surface-adsorbed $^3O_2$ to form a transient negative ion, $^2O_2^-$, which is a highly reactive species capable of oxidizing a variety of organic molecular adsorbates on the nanoparticle surfaces.[35] Therefore, the molecular O_2 in air could act as an efficient hot electron acceptor to drive the oxidative *p*ATP coupling reaction through a hot electron-mediated mechanism. The formation of DMAB could be effectively inhibited when the Au nanoparticles were coated with a thin dielectric shell of SiO_2 (Fig. 2F), which blocked the transfer of hot electrons from the Au nanoparticles to the surface-adsorbed O_2. In an O_2-free environment, direct oxidation of surface-adsorbed *p*ATP by the plasmonic hot holes generated through Landau damping becomes the only possible reaction pathway. However, the hot hole-driven reaction in the N_2 atmosphere was found to be kinetically so slow that the formation of DMAB became almost unobservable (Fig. 2D), suggesting that the plasmonic hot electrons were remarkably more efficient than the hot holes in catalyzing the oxidative coupling of the *p*ATP molecules residing in the nanoparticle-film junctions.

The hot electron-driven *p*ATP coupling under aerobic reaction conditions is a multistep process involving the photoexcitation of hot electrons, photo-activation of surface-adsorbed O_2, oxidation of surface-adsorbed *p*ATP by photo-activated O_2^-, and the formation of the N=N bonds in DMAB molecules. While the photoexcitation and transfer of hot electrons occur rapidly on time-scales of fs–ps,[31–34] the photocatalytic coupling of *p*ATP on Ag nanoparticle surfaces was observed to span drastically longer time-scales typically in the range of seconds to minutes,[119] strongly suggesting that there must be a rate-limiting kinetic bottle-neck associated with the interfacial molecular transformations. Zhang *et al.*[119] found that the rate-limiting step for the hot electron-driven DMAB formation under the continuous-wave (cw) laser excitations was associated with the thermal reactions between photo-activated O_2^- and surface-adsorbed thiophenol derivatives rather than the interfacial transfer of plasmonic hot electrons. In this work, SERS-based kinetic measurements were performed on individual SiO_2@Ag core-satellites supra-nanoparticles (SNPs) using a confocal Raman microscope (Fig. 3A and B). Each SNP was assembled by

densely decorating the surface of a dielectric SiO_2 bead with Ag nanocubes (Fig. 3C). The as-assembled SNPs displayed a broad plasmon resonance band in the near-infrared due to strong plasmon coupling between adjacent Ag nanocubes. Upon plasmonic excitations at 785 nm, the local electric fields were drastically enhanced inside the junctions between neighboring Ag nanocubes, creating hot spots for both Raman signal enhancement and surface accumulation of hot electrons. Although involving multiple steps, this photocatalytic reaction obeyed a surprisingly simple, first-order rate law (Fig. 3D–F). The apparent first-order rate constant, k, and the maximum reaction yield, $\theta_{t=\infty}$, were obtained by fitting the temporal evolution of the apparent fraction of DMAB, θ_{DMAB}, with a first-order rate equation. The reaction kinetics could be interpreted in the context of the following reaction mechanism, which involved photo-activated oxygen at its steady state concentrations.

$$O_2^{ad} \underset{-e^-, k_{-1}}{\overset{+\text{hot } e^-, k_1}{\rightleftharpoons}} O_2^-$$

$$O_2^- + \text{4-ATP} \xrightarrow{k_2} \text{TI}^* \xrightarrow{\text{fast}} 1/2\text{DMAB}$$

Here, k_1 was the rate constant for the photo-activation of surface adsorbed O_2, denoted as O_2^{ad}, upon transfer of a hot electron from Ag to O_2. k_{-1} was the rate constant for the reverse, thermal deactivation process. Both the photo-activation and thermal deactivation of O_2^{ad} were much faster than the formation of DMAB, rapidly establishing an equilibrium and keeping the photo-activated O_2^- at its steady

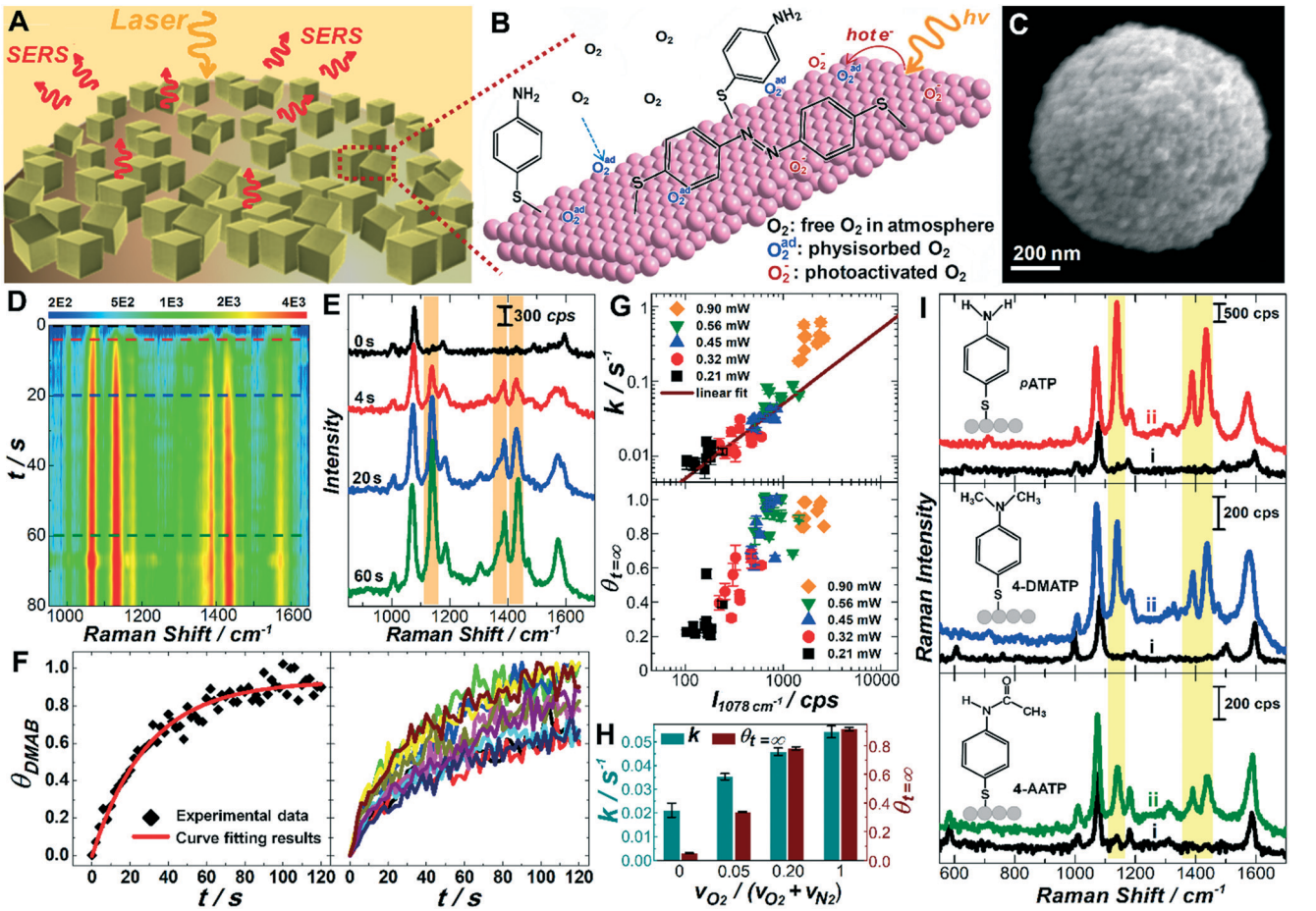

Fig. 3 (A) Schematic illustration of SERS measurements performed on individual SNPs composed of a SiO_2 core and Ag nanocube satellites. (B) Schematic illustration of plasmon-driven coupling of *p*ATP adsorbed on Ag surface in an aerobic reaction environment. (C) SEM image of a SiO_2@Ag SNP. (D) Time-resolved SERS spectra collected on one *p*ATP-coated SiO_2@Ag SNP upon exposure to 785 nm laser illumination in ambient air. The spectral acquisition time was 2 s and the laser power was 0.45 mW. (E) Snapshot SERS spectra collected at reaction times of 0, 4, 20, and 60 s. The highlighted peaks at 1440, 1390, and 1140 cm^{-1} are spectral signatures of DMAB. (F) Temporal evolution of θ_{DMAB} obtained from the time-resolved SERS results shown in panel D on one SiO_2@Ag SNP (left panel) and θ_{DMAB} trajectories collected on 10 different SiO_2@Ag SNPs under identical experimental conditions (right panel). The least-squares curve fitting results are shown as solid curve in the left panel. (G) Plots of k and $\theta_{t=\infty}$ *vs.* the initial SERS intensity of the C–S stretching mode at 1078 cm^{-1}, $I_{1078cm^{-1}}$, obtained from individual SiO_2@Ag SNPs at different excitation laser powers. (H) The values of k and $\theta_{t=\infty}$ at different O_2 partial pressures (785 nm, 0.45 mW). (I) SERS spectra of *p*ATP, 4-DMATP, 4-AATP adsorbed on SiO_2@Ag SNPs (i) before and (ii) after laser illumination (785 nm, 0.90 mW) for 120 s. Reprinted with permission from ref. 119. Copyright 2018, American Chemical Society.

state concentration. The O_2^- subsequently reacted with the surface-adsorbed *p*ATP to initiate the oxidative coupling reactions. The rate of DMAB formation was determining by a rate-limiting step with a rate constant of k_2, which was most likely associated with the formation of a partially dehydrogenated transient intermediate, denoted as TI*. Within this steady state kinetic model, the apparent first-order rate constant, k, was related to k_1, k_{-1}, k_2, and the interfacial abundance of surface-adsorbed O_2, $[O_2^{ad}]$, as described by the following equation

$$k = k_2 \frac{k_1}{k_{-1}} \left[O_2^{ad}\right].$$

The overall rates of DMAB production could be fine-tuned by varying k_1, k_2, and $[O_2^{ad}]$. k_1 could be experimentally modulated by either adjusting the excitation laser power or varying the local field enhancements in the plasmonic hot spots (Fig. 3G). The time-resolved SERS measurements enabled quantitative correlation between the reaction rates and the local field intensities on the surfaces of the photocatalysts. The rate constants varied linearly with the fourth power of the local fields at low excitation powers, but switched to a superlinear dependence when the excitation power exceeded certain threshold values, strongly suggesting further kinetic enhancement caused by the plasmonic photothermal heating. Both the rate of DMAB formation and the reaction yield could also be modulated by adjusting the partial pressure of O_2 in the reaction atmosphere, which controlled $[O_2^{ad}]$ on the photocatalyst surfaces (Fig. 3H). k_2 was intimately tied to the structures of the reactant molecules adsorbed on the plasmonic photocatalysts, changing significantly when substituting the amine group of *p*ATP with a dimethylamine or a acetylamine group. As shown in Fig. 3I, *p*ATP, 4-dimethylamino-thiophenol (4-DMATP), and 4-acetamido-thiophenol (4-AATP) all underwent plasmon-driven oxidative coupling processes to produce DMAB during SERS measurements. However, the reaction rates varied significantly, following the trend of *p*ATP > 4-DMATP > 4-AATP under identical reaction conditions. The difference in the reaction rates among the three thiophenol derivatives could be interpreted as the consequence of the different polarities and dissociation energies of the chemical bonds connected to the N atoms. In addition to the N=N bond formation in DMAB, a major side outcome of the plasmon-driven oxidative coupling of surface-adsorbed *p*ATP derivatives is the site-selective cleavage of the N–C bonds, which results in the release of the molecular units conjugated to the amine group from the nanoparticle surfaces. As demonstrated by Camden and coworkers,[120] such plasmon-driven N–C bond-scissoring processes could be adopted to develop a light-triggered approach to molecular delivery and release.

Without the involvement of additional hot carrier transfer channels, the plasmon-driven oxidative coupling of *p*ATP in O_2-free reaction environments appeared kinetically sluggish. However, this reaction could also occur through an alternative hot hole-driven pathway, kinetically boosted upon efficient charge separation when the metal nanostructures were in contact with electron acceptors. As shown in Fig. 4A–C, *p*ATP underwent rapid oxidative coupling reactions to produce DMAB on the surfaces of Ag–TiO_2 heteronanostructures under standard conditions for SERS measurements even in an atmosphere of pure N_2.[121] The kinetic enhancement originated from the efficient transfer of plasmonic hot electrons from Ag to TiO_2, benefiting from the close energy match between the conduction band of TiO_2 (−4.05 eV *vs.* vacuum) and the Fermi level of Ag (−4.3 eV *vs.* vacuum). Plasmonic photothermal heating at the nanocatalyst surfaces, in principle, may also provide sufficient energy to overcome such a small energy barrier for the electron transfer from Ag to TiO_2. However, neither the surface temperature of the photocatalysts during the reactions nor the kinetics of the dark reactions at elevated temperatures was further investigated in this work.[121] Therefore, how the photothermal effects influence the reaction rates still remains unclear and open to further investigations.

Such charge separation led to prolonged life-times of the hot holes in the Ag nanoparticles, which triggered the electron transfer from surface-adsorbed *p*ATP to the Ag nanoparticles to boost the oxidation of *p*ATP (Fig. 4A). The separation of hot electrons and holes could also be promoted using electron scavengers, such as $AgNO_3$.[122] As shown in Fig. 4D, the presence of $AgNO_3$ in the reaction media significantly enhanced the kinetics of the coupling reactions in an N_2 atmosphere. When both $AgNO_3$ and O_2 were present, DMAB could be further oxidized to form *para*-nitrothiophenol (*p*NTP) during SERS measurements, as evidenced by the emergence of the characteristic Raman peak of the nitro group at 1328 cm^{-1} (Fig. 4F).

Besides transferring hot electrons to semiconductors or electrons scavengers, the interfacial charge separation of plasmonic hot carriers could also be promoted by surface-capping molecular ligands. Habteyes and coworkers[123] studied the aerobic oxidative coupling of *p*ATP in the junctions between a substrate and Au nanorods coated with various ligands. Fig. 4G shows the SERS results along with the cartoons illustrating the reactants and surface ligands in the nanorod-substrate junctions. Use of citrate-capped Au nanorods as the plasmonic photocatalysts resulted in the formation of DMAB, whereas switching the ligands on Au nanorods from citrate to cetyltrimethylammonium bromide (CTAB) led to efficient oxidation of *p*ATP into *p*NTP. When the *p*ATP molecules were directly adsorbed on the Au nanorod surfaces, *p*ATP was selectively oxidized into DMAB without any detectable *p*NTP. Strong correlation was observed between the N–O and Au–Br vibrational band intensities, suggesting that the bromide anions in CTAB served as a hole-scavenger to promote the charge separation and thus effectively enhanced the hot electron-driven oxidation reactions. This work clearly demonstrated an important proof-of-concept that the selectivity of plasmon-driven oxidation reactions could be enhanced through judicious selection of surface-capping ligands on the photocatalyst surfaces.

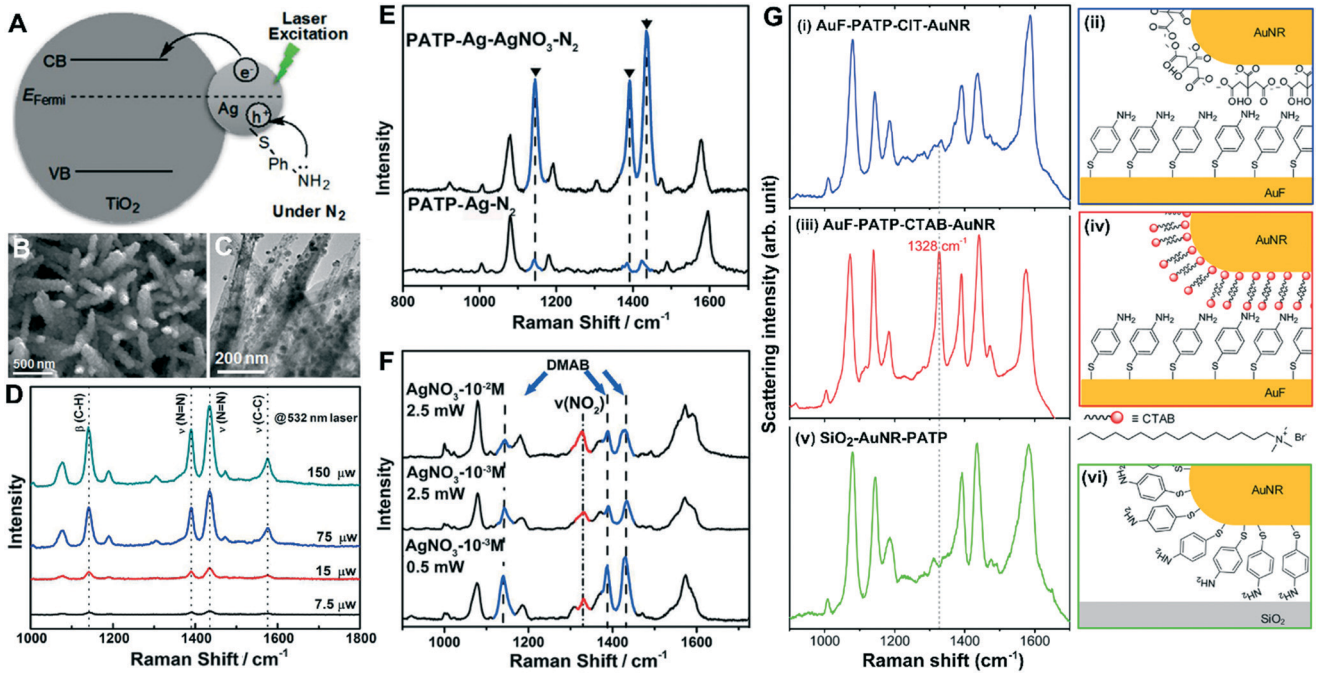

Fig. 4 (A) Proposed mechanism of hot hole-driven oxidative coupling of *p*ATP on the surface of Ag–TiO_2 heteronanostructures in an N_2 atmosphere. (B) SEM and (C) TEM image of Ag–TiO_2 heteronanostructures composed of TiO_2 nanowhiskers decorated with Ag nanoparticles. (D) SERS spectra of *p*ATP on Ag–TiO_2 heteronanostructures illuminated by a 532 nm cw laser at different laser powers. Reprinted with permission from ref. 121. Copyright 2016, John Wiley and Sons. (E) Comparison of SERS spectra of *p*ATP on Ag nanoparticles with $AgNO_3$ and without $AgNO_3$ in an N_2 atmosphere illuminated by a 532 nm laser. (F) SERS spectra of *p*ATP on Ag nanoparticles illuminated by a 532 nm laser at various excitation powers when both $AgNO_3$ and atmospheric O_2 are present. Reprinted with permission from ref. 122. Copyright 2016, Springer Nature. (G) SERS spectra and schematic illustration of *p*ATP in various local chemical environments with 633 nm excitations. The *p*ATP molecules were located in junctions between (i and ii) citrate-capped Au nanorods and Au film; (iii and iv) CTAB-capped Au nanorods and Au film; (v and vi) *p*ATP-coated Au nanorods and SiO_2 substrates. Reprinted with permission from ref. 123. Copyright 2017, American Chemical Society.

3.2 Plasmon-driven reduction of *p*NTP

The plasmon-driven reductive coupling of *p*NTP adsorbed on nanostructured metal surfaces provides an alternative approach to the photocatalytic synthesis of DMAB.[104,105,124] For example, Wang and coworkers[125] observed that *p*NTP molecules adsorbed on Ag particles underwent a plasmon-driven reductive coupling reaction to form DMAB (Fig. 5A). In this case, individual micron-sized Ag particles with highly roughened surfaces (Fig. 5B) were used to serve as both the plasmonic photocatalysts and the SERS substrates. The plasmonic field enhancements on the roughened particle surfaces were significantly higher than those achievable on individual spherical Ag nanoparticles. As shown in Fig. 5C, the molecular transformations during plasmon-driven reductive coupling of *p*NTP could be resolved with great detail by the time-resolved SERS spectra collected from molecules adsorbed on the open surfaces of individual surface-roughened Ag particles without the involvement of the gap-mode hot spots confined within either the interparticle junctions or the nanoparticle-film junctions. The SERS spectral features of *p*NTP adsorbed on Ag were dominated by three major peaks, the nitro stretching mode (ν_{NO_2}) at 1335 cm^{-1}, the C–S stretching mode (ν_{CS}) at 1076 cm^{-1}, and the benzene ring mode (ν_{ring}) at 1580 cm^{-1}. When illuminated by a 532 nm cw laser at an excitation power of 0.5 W, the intensity of the ν_{NO_2} peak progressively decreased while the characteristic peaks of DMAB at 1140, 1380, and 1440 cm^{-1} became increasingly more intense, signifying the conversion of *p*NTP to DMAB. At 633 nm excitations, the same reaction also occurred but proceeded at significantly slower rates than at 532 nm excitations. Colloidal Cu nanoparticles could also serve as highly active plasmonic photocatalysts for the reductive coupling of *p*NTP with seemingly even higher catalytic efficiencies than colloidal Ag at both 532 and 633 nm excitations.[126] As shown in Fig. 5D and E, *p*NTP molecules in Cu sols were completely converted to DMAB as evidenced by the disappearance of the ν_{NO_2} peak in the SERS spectra, whereas both *p*NTP and DMAB coexisted on the surfaces of Ag colloids under the same set of reaction conditions. The SERS spectral features of the DMAB produced from the reductive coupling of *p*NTP in Cu sol were in excellent agreement with those of the DMAB generated from the oxidative coupling of *p*ATP in Ag sol (Fig. 5F).

The plasmon-driven reductive coupling of *p*NTP is initiated upon the transfer of a hot electron from the metal nanostructure to the LUMO of a surface-adsorbed *p*NTP molecule, which leads to the formation of a transient negative ion denoted as *p*NTP$^{\bullet-}$ at the early stage of the reaction.[127] Therefore, the reaction mechanism is strikingly

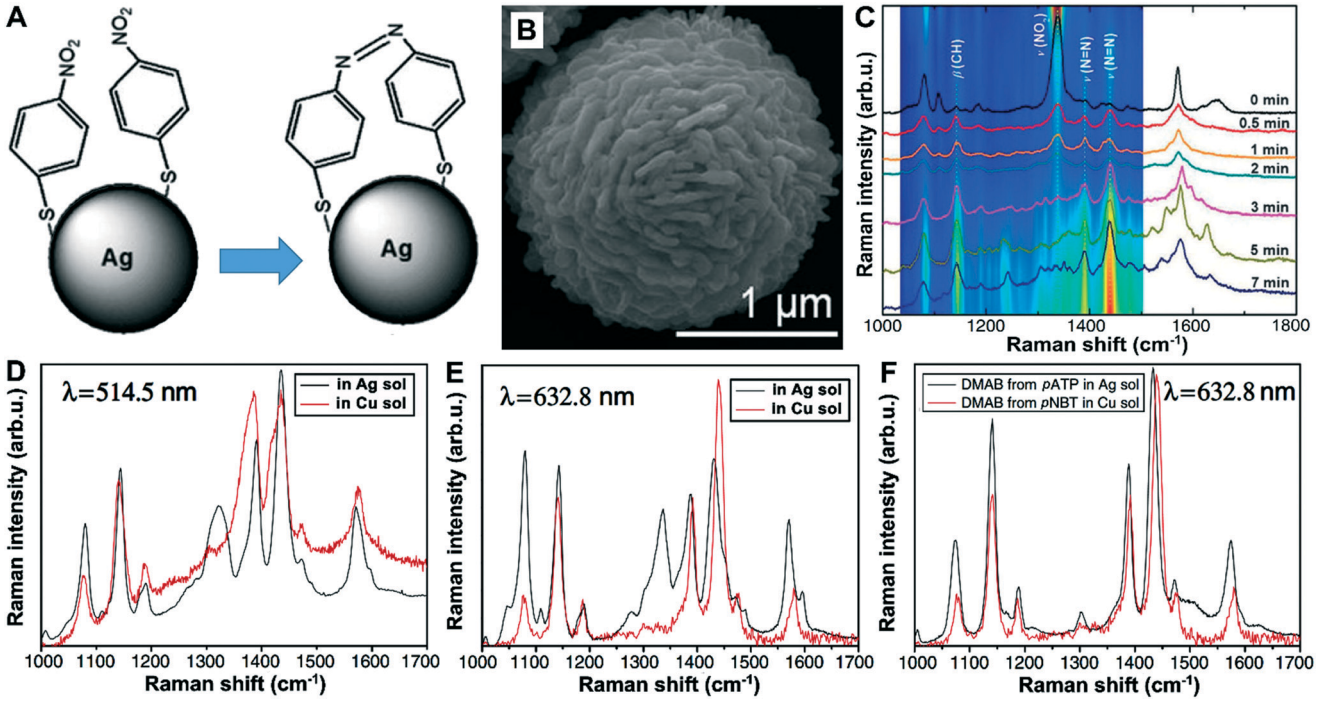

Fig. 5 (A) Scheme illustrating the formation of DMAB through plasmon-driven reductive coupling of *p*NTP adsorbed on Ag nanoparticle surfaces. (B) SEM image of an individual surface-roughened Ag particle. (C) Temporal evolution of SERS spectra collected on an individual *p*NTP-coated surface-roughened Ag particle. Selected SERS spectra at several reaction times were plotted. All spectra were collected at 532 nm excitations (0.5 mW) with an integration time of 2 s. The spectra were off-set for clarity. Reprinted with permission from ref. 125. Copyright 2013, The Royal Society of Chemistry. SERS spectra of *p*NTP in Ag and Cu sols at excitation wavelengths of (D) 514.5 nm and (E) 632.8 nm. (F) SERS spectra of DMAB produced from *p*ATP in Ag sol and from *p*NTP in Cu sols at an excitation wavelength of 632.8 nm. Reprinted with permission from ref. 126. Copyright 2011, John Wiley and Sons.

different from that of the oxidative coupling of *p*ATP mediated by hot electron acceptors, such as O_2, despite the fact that both reactions lead to the same product, DMAB. The LUMO energy of a *p*NTP molecule chemisorbed on Ag surface was calculated to be ~1.7 eV above the Fermi level of Ag.[128] The generation of hot electrons with sufficient energies to get injected into the LUMO of surface-adsorbed *p*NTP requires the use of visible light with photon energies greater than 1.7 eV (wavelength < 720 nm) for plasmonic excitations. At the same excitation power densities, the reaction rates at 532 nm excitations were observed to be drastically faster than those at 633 nm excitations on Ag nanoparticles, because shorter-wavelength excitations created hot electrons that were distributed over a broader energy range above the Fermi level of Ag, which resulted in larger fraction of energetic hot electrons exploitable for driving the reactions. Such excitation wavelength-dependence was also observed in TERS measurements performed on *p*NTP molecules in the junctions between an Ag-coated tip and Au nanoplates.[129]

Time-resolved SERS results suggested the formation of the $pNTP^{\bullet-}$ intermediate at the early stage of the plasmon-driven reduction of *p*NTP. Kim and coworkers[127] conducted detailed kinetic studies on the photocatalytic reduction of *p*NTP molecules located inside a plasmonic junction between a Ag nanoparticle (AgNP) and a Au thin-film (AuTF) under cw laser illumination at an excitation wavelength of 633 nm (Fig. 6A). They observed that the NO_2-stretching (ν_{NO}) peak showed a rapid spectral down-shift by ~6 cm^{-1} within ~2 s immediately after the initiation of the reaction, while the intensity of the peak kept essentially unchanged (Fig. 6B–D). During such a period, the formation of DMAB was also delayed. After the initial step, the intensity of the ν_{NO} peak started to decrease gradually, accompanied by the emergence of the characteristic peaks of DMAB. The spectral down-shift of the ν_{NO} peak at the initial stage of the reaction was consistently observed when repeating the same SERS measurements at different junction sites on the substrates, and a histogram showing the distribution of the ν_{NO} shift ($\Delta\nu$) was displayed in Fig. 6E. The site-to-site deviations of $\Delta\nu$ were most likely due to the intrinsic variation of the local-field intensities and the detailed structural features among different junction-defined hot spots. A Gaussian function was used to fit the distribution and the full width at half maximum (FWHM) of this distribution was determined to be 1.7 cm^{-1}. With the proposed hot electron injection mechanism in mind, the initial spectral down-shift was hypothesized to be an indication of the formation of a $pNTP^{\bullet-}$ anion radical, which was derived from the injection of a single hot electron into the LUMO of a surface-adsorbed pNTP molecule. To further test this hypothesis, the *p*NTP molecules adsorbed on Ag electrodes were electrochemically reduced and SERS spectra were collected at different electrode potentials. When periodically switching the electrode potentials between

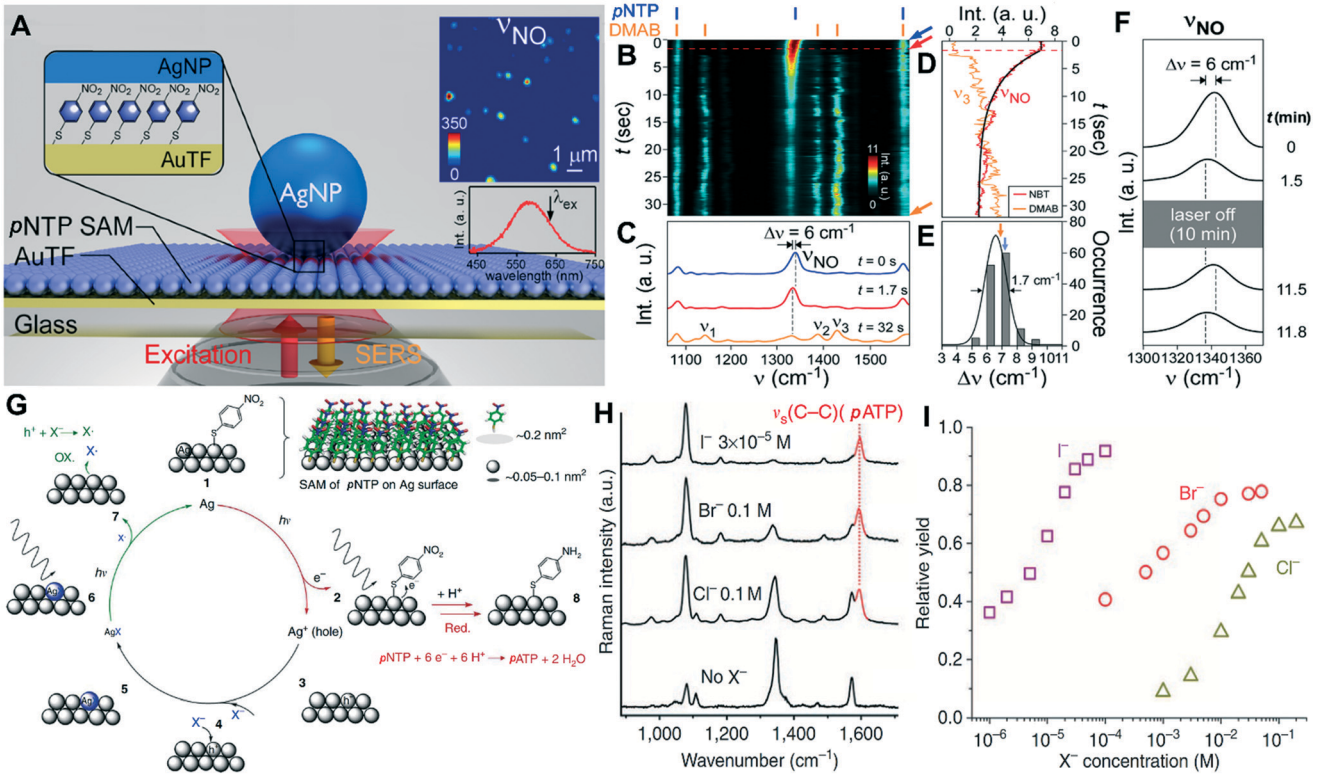

Fig. 6 (A) Schematic illustration of an AgNP/*p*NTP/AuTF junction. The inset is a SERS image of the intensity of ν_{NO} at different junctions. The inset spectrum represents a plasmon scattering spectrum measured by a dark-field spectromicroscope. The excitation wavelength was 633 nm, which is indicated by the black arrow. (B) Temporal evolution of SERS spectra during reductive coupling of *p*NTP molecules at an AgNP/*p*NTP/AuTF junction. (C) The representative spectra at different time points: 0, 1.7, and 32 s. The shift of the ν_{NO} peak is indicated by the dotted line. (D) The trace of ν_{NO} and ν_3 (representing DMAB) over time. (E) Histogram of the shift of ν_{NO} (grey bars) and the Gaussian function fitting results (black curve). (F) The illustration of the effect of temporarily blocked laser beam (laser off, 10 min) on the temporal evolution of the ν_{NO} peak positions. Reprinted with permission from ref. 127. Copyright 2016, American Chemical Society. (G) Schematic illustration of plasmonic hot electron-driven *p*NTP reduction with the aid of halide ions as co-catalysts. (H) The final SERS spectra of *p*ATP on Ag co-catalyzed by different halide ions, I^-, Br^-, Cl^-. (I) The relative yield of reduction reaction in the presence of different halide ions at various concentration. Reprinted with permission from ref. 132. Copyright 2015, Springer Nature.

−0.2 and −1.2 V *vs.* Ag/AgCl, a reversible spectral shift of the ν_{NO} peak by 7 cm^{-1} was observed, signifying the reversible reduction and oxidation of the *p*NTP molecules. The results of quantum mechanical calculations also showed that the injection of an electron into a *p*NTP molecule could indeed cause the spectral down-shift of the ν_{NO} peak. Besides the electrochemical approach, the spectral shift of the ν_{NO} modes could also be modulated through alternating laser illumination and thermal relaxation in dark (Fig. 6F). Upon laser illumination of the samples, the down-shift of ν_{NO} was consistently observed, whereas the ν_{NO} peak shifted back to its original peak position in a fully reversible manner once the illumination laser was blocked. Although the down-shift of the ν_{NO} peak might also be associated with photothermally induced conformational changes of *p*NTP, all the experimental observations mentioned above coherently suggested that the spectral down-shift of the ν_{NO} Raman peak was most likely caused by the hot electron injection into the *p*NTP molecules. Therefore, the formation of the $pNTP^{\bullet-}$ anion radicals was identified as a critical elementary step at the initial stage of the plasmon-driven reduction of *p*NTP. The formation of $pNTP^{\bullet-}$ anion radicals was further confirmed by El-Khoury and coworkers through TERS measurements.[130] More recently, Schürmann and coworkers[131] characterized the formation yield of anionic species as a function of the electron energy through gas-phase crossed electron-molecular beam measurements. Schürmann's experiments can be considered as an electron beam-driven analog to the plasmon hot electron-driven reduction of *p*NTP, providing important implication that helps the assessment of the accessibility of various reduction pathways following the initial electron transfer from the plasmonic nanoparticles to the molecular adsorbates.

Although the photocatalytic reduction of *p*NTP was driven by plasmonic hot electrons, the hole-mediated oxidation counter-half-reactions should also be taken into considerations. Xie and Schlücker[132] discovered that a halide-assisted oxidation counter-half-reaction effectively promoted the photocatalytic reduction of *p*NTP on Ag surfaces without the need to introduce any additional chemical reducing agents. In this case, hot electrons were generated in Ag nanoparticles through Landau damping and then transferred to *p*NTP adsorbed on the Ag surface to initiate a stepwise

reduction process that eventually led to formation of *p*ATP. Protons served as the hydrogen source and halide anions reacted with the electron-donating Ag to form a transient silver halide adlayer on the Ag surface, which underwent photo-dissociation during the reactions to regenerate Ag surfaces to complete the catalytic reaction cycles (Fig. 6G). The halide anions worked as a co-catalyst mediating the hot hole-driven oxidation half-reactions, while the reduction half-reactions were dictated by the hot electrons. As shown in Fig. 6H, with the aid of halide anions, the final outcome of the plasmon-driven photocatalytic *p*NTP reduction was a six electron-reduction product, *p*ATP, instead of the two electron-reduction product, DMAB. The reaction yields varied significantly when changing the types and concentrations of the halide cations in the reaction media (Fig. 6H and I). The catalytic efficacy of the three halide anions decreased in the order of $I^{-1} > Br^{-1} > Cl^{-1}$, and this trend could be interpreted in the context of the relative solubility and photosensitivity of the corresponding silver halide salts.

It is believed that *p*NTP can be reduced into *p*ATP through two possible reaction pathways: (1) an unimolecular pathway in which *p*NTP is reduced in a stepwise manner involving the sequential formation of several intermediates, including dihydroxylaminobenzenethiol (DHABT), nitrosobenzenethiol (NSBT), and hydroxylaminobenzenethiol (HABT); (2) a bimolecular pathway involving the coupling between the DHABT and HABT intermediates to yield DMAB, followed by further reduction to form *p*ATP. However, it remains challenging to distinguish these two mechanisms through spectroscopic measurements performed at the ensemble level due to the ensemble-averaging of the spectroscopic signals. Taking full advantage of its single-molecule detection

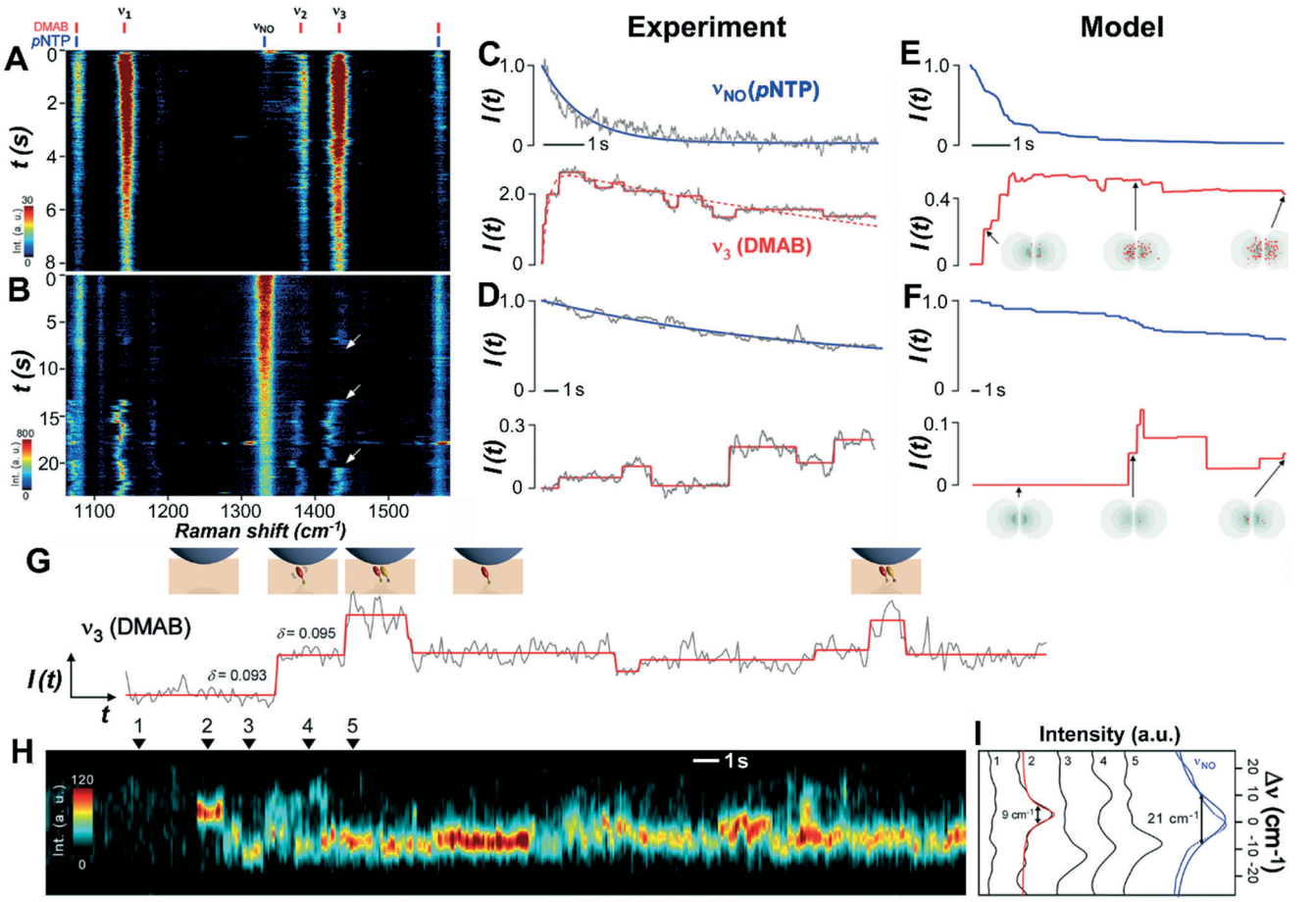

Fig. 7 (A and B) Time-resolved SERS spectra of *p*NTP in two different AgNP/*p*NTP/AuTF junctions at 633 nm excitations. White arrows in panel B point to the discrete changes in the SERS intensities of ν_3 (DMAB). The peak assignments of *p*NBT (blue) and DMAB (red) were shown at the top of panel A. (C and D) Time-resolved SERS intensities (gray) of ν_{NO} (*p*NBT) and ν_3 (DMAB) peaks sampled from the results shown in panels A and B, along with the fit to a single exponential function (blue) and step function (red). The dotted red trace in panel C is the fit to a rise-and-decay rate equation, showing that the envelope of the DMAB trajectory approximately follows the ensemble kinetics. The intensities were normalized with respect to the initial SERS intensity of the ν_{NO}. (E and F) Model SERS trajectories of ν_{NO} (*p*NBT, blue) and ν_3 (DMAB, red). The inset cartoons in panels E and F display snapshots of the DMAB distributions (red dots) and the local field distribution (green) inside the AgNP/*p*NTP/AuTF junctions. (G) Normalized SERS trajectory of DMAB (gray) and the fit to step functions (red) and (H) the associated time-resolved SERS spectra. (I) Sampling of the instantaneous spectra of ν_3 (DMAB) (indicated by numerals in panel H) together with fits to Lorentzian functions. The inset cartoons in panel G schematically show the evolution of the number of DMAB molecules (red and orange spheroids) during the reaction. Reprinted with permission from ref. 133. Copyright 2016, American Chemical Society.

sensitivity, Kim and coworkers[133] used SERS as an *in situ* spectroscopic tool to time-resolve detailed dynamic single-molecule events involved in plasmon-driven reduction of *p*NTP. They found that the temporal evolution of the SERS spectral features of surface-immobilized *p*NTP molecules residing in individual nanoparticle-thin film junctions displayed discrete step-transitions, which reflected the dynamics of single-molecule events in the plasmonic hot spots. Although the SERS trajectories for *p*NTP and DMAB were found to be temporally correlated, molecules in different junctions on the same substrate exhibited widely different, heterogeneous reaction kinetics. Fig. 7A and B show the representative time-resolved SERS spectra collected on individual junctions that were featured by a fast and a slow decay in the SERS peak intensity of *p*NTP, respectively. Fig. 7C and D show the corresponding SERS intensity trajectories of the ν_{NO} (*p*NTP) and ν_3 (DMAB) peaks during the plasmon-driven reactions at 633 nm excitations. The fast decay of the ν_{NO} peak could be fitted by a single-exponential decay function, and was accompanied by strong ν_3 (DMAB) peak intensities (Fig. 7C). In contrast, the slow *p*NTP decay was typically associated with weak intensities of the ν_3 (DMAB) peak (Fig. 7D). While the *p*NTP trajectories decayed continuously over time, the DMAB trajectories showed discrete, step-like transitions. Such step-transitions were particularly notable in the slow *p*NTP-decaying cases (Fig. 7B and D), in which the intensities of the ν_3 (DMAB) peak showed numerous on/off transitions, which could be attributed to the creation and annihilation of individual DMAB molecules within individual plasmonic hot spots. The temporal evolution of the SERS spectral features reflected single-molecule reaction kinetics, suggesting that the majority of *p*NTP molecules were reduced into *p*ATP through an unimolecular reaction path rather than through the DMAB-forming bimolecular pathway. Although the formation of DMAB was a minority event during the reactions (<10%), the SERS spectral features of DMAB could still be well-resolved because the Raman cross sections of DMAB were significantly larger than those of *p*NTP and *p*ATP. All the experimentally observed spectral features could be well-reproduced by a model, in which both the plasmonic field enhancements and the surface photochemistry were taken into considerations (Fig. 7E and F). The stepped transitions of DMAB were also found to be correlated with the changes in spectral lineshapes. As shown in Fig. 7G and H, some stepped jumps in SERS intensities were accompanied by spectral changes between a singlet and doublet peaks, strongly suggesting that the step-transitions corresponded to chemical transformations of one of the two DMAB molecules in the same hot spots. The singlet peak was significantly narrower than that of the heterogeneously broadened ensemble ν_{NO} peak (Fig. 7I), indicating that the SERS spectral signals were collected from single or a few DMAB molecules in each hot spot. This work clearly demonstrates the feasibility of using SERS as a single-molecule spectroscopic tool to differentiate various reaction pathways and fully resolve the intermediate dynamics during plasmon-driven photocatalytic reactions.

When the excitation photon energies are sufficiently high, the plasmon-driven reduction of *p*NTP is initiated primarily by the injection of hot electrons into the LUMO of the surface-adsorbed *p*NTP. On Ag substrates, this metal-to-adsorbate transfer of hot electrons requires an excitation energy above 1.7 eV (wavelength < ~720 nm).[107] When using Au nanostructures as the plasmonic photocatalysts, the threshold excitation energy becomes even higher because the Fermi level of Au lies ~0.7 eV further below that of Ag.[107] Surprisingly, the reductive coupling of *p*NTP can still occur rapidly under certain reaction conditions even at excitation energies far below the energy gap between the Fermi levels of the metals and the LUMO of surface-adsorbed *p*NTP,[134–137] strongly implying that there must be certain types of hot carrier-relaying species existing in the reaction media that can effectively mediate the *p*NTP reduction through alternative hot carrier transfer channels. Zhang *et al.*[137] conducted detailed SERS-based kinetic studies on the plasmon-driven reductive coupling of *p*NTP chemisorbed on Fe_3O_4-supported Ag nanocube aggregates under near-infrared excitations (λ_{ex} = 785 nm) in a series of controlled reaction atmospheres. They found that surface-adsorbed molecular oxygen played a unique role as an interfacial charge carrier-relaying co-catalyst during the multistep *p*NTP coupling reactions. Signified by an induction time at the initial stage followed by the DMAB formation obeying an apparent first-order rate law, the O_2-mediated reductive coupling of *p*NTP on Ag under near-infrared laser excitations exhibited unique kinetic features that were significantly different from those of the reactions under visible laser excitations (Fig. 8A). When increasing the excitation power density, both the overall reaction rates and the yields of DMAB increased, but the induction time was shortened until it became no longer resolvable experimentally above certain power density thresholds (Fig. 8B). The SERS-based kinetic measurements conducted on individual Fe_3O_4@Ag nanocubes core-satellites particles provided a unique way to correlate the reaction kinetics with the local-field intensities in the plasmonic hot spots, which were assessed based on the initial SERS intensities of the ν_{NO_2} peak of *p*NTP. As shown in Fig. 8C–E, the apparent first-order rate constant (k), the duration of the induction time (t_{ind}), and the maximum reaction yield ($\theta_{t=\infty}$) were all strongly correlated to the initial SERS intensities of the ν_{NO_2} peak. The results of DFT calculations showed that although the hot electrons generated under 785 nm excitations were not energetic enough to get injected into the LUMO of *p*NTP, they could be readily transferred into O_2 because of the nearly perfect alignment of the antibonding $2\pi^*$ orbital of the surface adsorbed O_2 with the Ag Fermi level (Fig. 8F). The hot electron transfer from metals to surface-adsorbed O_2 results in the formation of transient O_2^- radicals, which can rapidly pass an electron onto surface-adsorbed *p*NTP to initiate the reductive coupling reaction and regenerate O_2. Meanwhile, the electrons in the $2\pi^*$

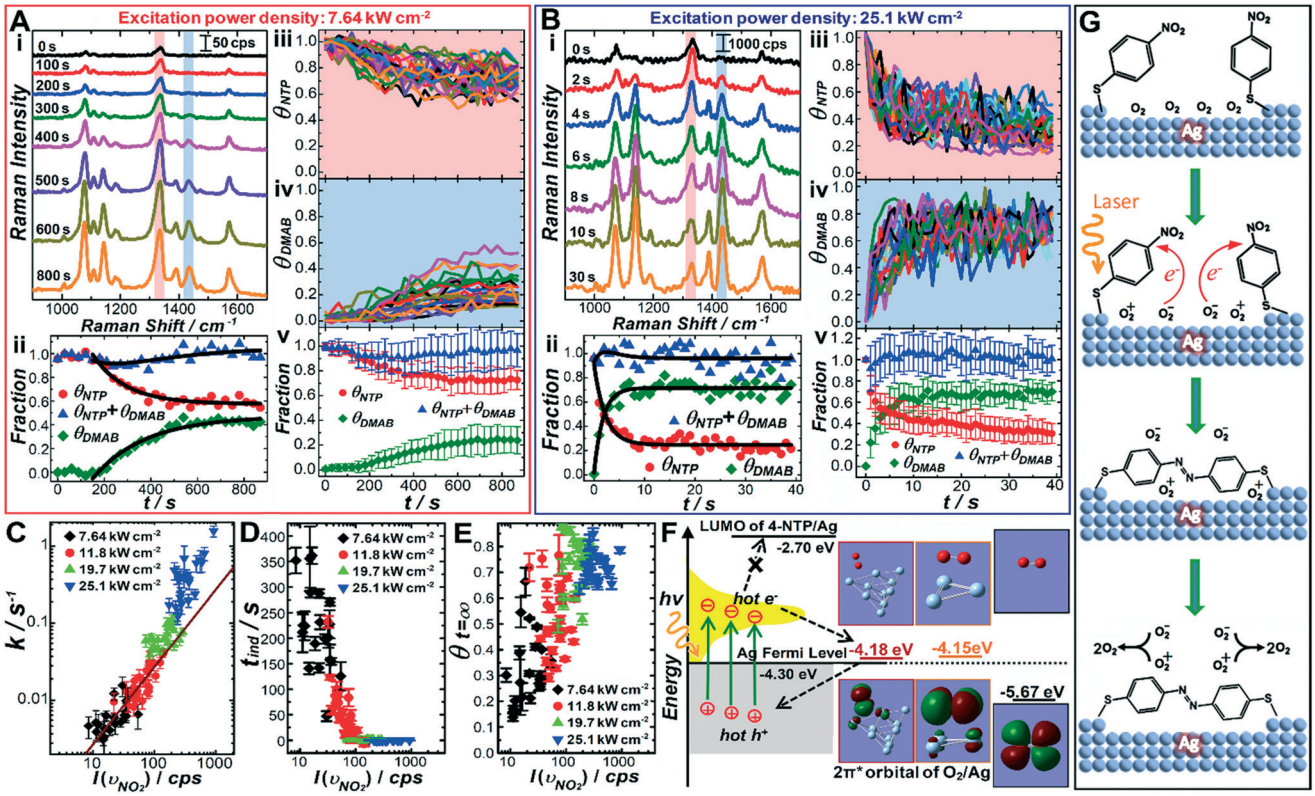

Fig. 8 Temporal evolutions of (i) SERS spectra and (ii) θ_{NTP}, θ_{DMAB}, and θ_{DMAB} + θ_{NTP} trajectories on a single *p*NTP-coated Fe_3O_4@Ag nanocubes core-satellites SNP, trajectories of (iii) θ_{NTP} and (iv) θ_{DMAB} collected on different individual *p*NTP-coated Fe_3O_4@Ag SNPs, and (v) ensemble-averaged θ_{NTP}, θ_{DMAB}, and θ_{DMAB} + θ_{NTP} trajectories at 785 nm excitation with an excitation power density of (A) 7.64 and (B) 25.1 kW cm^{-2}. Plots showing the correlation of (C) *k*, (D) t_{ind}, and (E) $\theta_{t=\infty}$ to the initial intensity of the ν_{NO2} peak in the SERS spectra. All the data were acquired at 785 nm excitations with four different excitation power densities as labeled in figures. (F) Energy diagram illustrating the plasmonic hot carrier transfer processes involved in the reductive coupling of *p*NTP aided by interfacial O_2 under near-infrared excitations. The energy levels of the 2π* of O_2 adsorbed on Ag atomic clusters were calculated by DFT. The energy diagram was plotted using an energy scale of electron volts (eV) and the vacuum level as the reference. The optimized geometries and the electron density maps of 2π* orbitals of a free O_2 molecule and an O_2 molecule adsorbed on an Ag_3 cluster and an Ag_{10} cluster were shown above and below the orbital energy levels, respectively. (G) Proposed mechanism of plasmon-driven aerobic reductive coupling of *p*NTP chemisorbed on Ag. Reprint with permission from ref. 137. Copyright 2019, American Chemical Society.

orbital of surface-adsorbed O_2 might also transfer to the Ag to combine with the plasmonic holes, preventing the Ag nanoparticles from photo-corrosion during the reactions. Both the interfacial O_2^- and O_2^+ radicals were short-lived, undergoing rapid recombination to form O_2, as schematically illustrated in Fig. 8G. In this plasmon-driven molecule-transforming process, O_2 essentially played a unique role as a hot carrier-relaying co-catalyst that worked synergistically with the plasmonic Ag photocatalysts. The reductive coupling of *p*NTP was found to be kinetically sluggish with negligible DMAB formation under near-infrared excitations in an anaerobic N_2 atmosphere, which was in striking contrast to the situations under visible excitations. When excited at 633 nm, the plasmon-driven reductive coupling of *p*NTP occurred rapidly on Ag nanoparticles in an N_2 atmosphere but became kinetically much slower in an O_2 atmosphere because O_2 competed with *p*NTP as a hot electron acceptor, which suppressed the hot electron injection into *p*NTP.[138] While both the experimental observations and DFT calculations suggest that surface-adsorbed O_2 played a crucial role as a hot carrier-relaying species during the plasmon-driven *p*NTP coupling reactions under near-infrared excitations, direct evidence verifying the formation of transient O_2^- and O_2^+ radicals on the nanoparticle surfaces is still needed to further validate the proposed mechanisms shown in Fig. 8G.

The time-resolved SERS results obtained from individual Fe_3O_4@Ag nanocubes core-satellites particles provided thought-provoking information that shed light on the effects of local-field enhancements and photothermal heating on the overall reaction kinetics. As clearly shown in Fig. 8C, the rate constant, *k*, increased with the local field intensity, which depends on both the field-enhancement in the hot spots and the power density of the excitation laser. The quantitative relationship between local-field enhancement and reaction rate, however, may vary drastically from system to system, sensitively depending on the structures of the photocatalysts and detailed reaction conditions. Brooks and Frontiera[134] found that the reaction kinetics appeared independent of the local field enhancement when the *p*NTP coupling reaction took place on the surfaces of Au-coated polystyrene nanospheres under near-infrared excitations. Such discrepancy in experimental observations implied that in

addition to the local-field enhancement, other factors could also play crucial roles in determining the reaction rates, and plasmonic photothermal heating was found to be one of them. The results of DFT calculations indicated that the plasmonic photothermal heating at the nanoparticle surfaces could provide sufficient thermal energies to overcome the energy barriers for the *p*NTP adsorbates to switch from metastable conformations to thermodynamically more favored conformations.[137] Ren and coworkers[139] recently found that the plasmonic reductive coupling of *p*NTP required specific geometric arrangements of *p*NTP molecule with respect to the metal surfaces. Photothermal heating was capable of triggering the conformational changes of molecule adsorbates, thereby activating the molecules for the reductive coupling reactions. Such photothermally induced conformational change of the surface-adsorbed *p*NTP was experimentally witnessed as the induction time prior to the initiation of the *p*NTP coupling reactions. At sufficiently high excitation powers, the t_{ind} values became vanishingly small (Fig. 8D) due to rapid photothermal heating at the nanoparticle surfaces. Also revealed by Fig. 8C was the superlinear dependence of k on the ν_{NO_2} peak intensity in the high excitation power density regime, which strongly suggested that the photothermal effect kinetically boosted the reactions at high excitation powers.

No consensus has been reached so far concerning to what extent the photothermal effect affects the overall reaction kinetics because it remains challenging to fully delineate the effects of photothermal heating and plasmonic hot carriers on the overall rates of the reactions. Using an ultrafast pump-probe SERS approach, Frontiera and coworkers[140] measured the local temperature of various vibrational modes of *p*NTP molecules residing in the plasmonic hot spots on Au nanoparticle aggregates. They found that the thermally deposited energy from nanoparticles to adsorbates was rapidly dissipated on the sub-100 ps time-scale, rendering a moderate temperature elevation at the nanoparticle-adsorbate interfaces. As shown in Fig. 9A, the Stokes and anti-Stokes Raman modes of *p*NTP in the plasmonic hot spots were resolved using a femtosecond pump pulse centered at 1035 nm to excite the plasmon resonances of the Au nanoparticle aggregates. The relations of Stokes and anti-

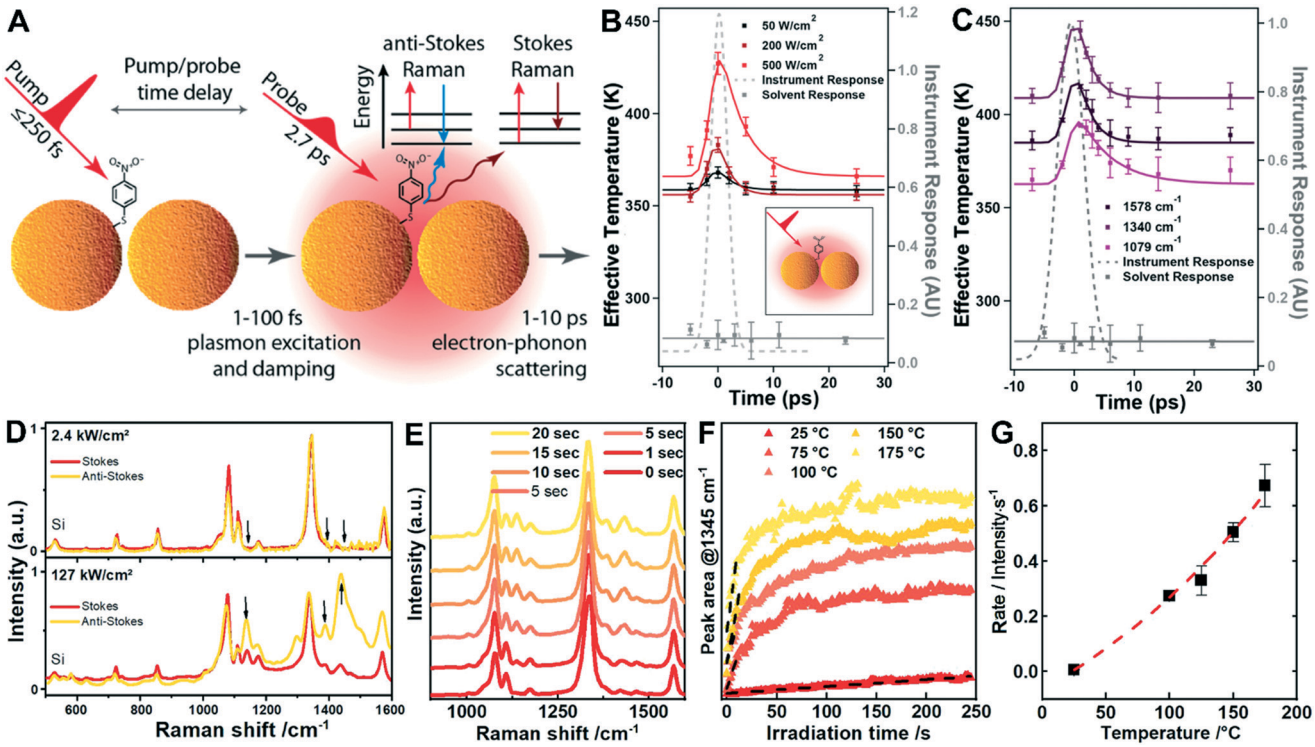

Fig. 9 (A) Schematic demonstration of using ultrafast pulse lasers to probe the vibrational temperatures of molecular adsorbates in interparticle junctions between Au nanoparticles. A picosecond probe pulse was used to obtain both the Stokes and anti-Stokes SERS spectra and the relative intensity of these two spectra gave the temperature that the molecules experienced. (B) The effective temperature of the *p*NTP molecules adsorbed on Au nanoparticles probed by different excitation power densities at an excitation wavelength of 1035 nm. The temperatures were obtained by analyzing intensities of Stoke at 1079 cm^{-1} and anti-Stokes at –1079 cm^{-1}. (C) The effective temperature of the *p*NTP molecules adsorbed on Au nanoparticles analyzed using different vibrational modes at an excitation power density of 200 W cm^{-2}. Reprinted with permission from ref. 140. Copyright 2018, American Chemical Society. (D) The Stokes and anti-Stokes SERS spectra of *p*NTP adsorbed on the surfaces of Au nanoflowers recorded with λ_{ex} of 785 nm laser at power densities of (upper panel) 2.4 and (lower panel) 127 W cm^{-2}. (E) Stokes SERS spectra of *p*NTP after different irradiation times with a laser power density of 25.5 W cm^{-2} at a bath temperature of 293 K. (F) Kinetics of the product extracted from the peak area at 1345 cm^{-1} at different bath temperatures. (G) Rates extracted from the kinetic results shown in panel F (fitting indicated in panel F by dashed lines) at various reaction temperatures. Reprint with permission from ref. 147. Copyright 2019, Springer Nature.

Stokes intensities of a certain vibrational mode were further extracted and analyzed to obtain information about the temperatures of that mode. Fig. 9B shows the excitation power density-dependent temperature elevation of the ν_{CS} mode at 1079 cm^{-1}. Fig. 9C compares the temperature elevations of three different vibrational modes, the ν_{C-S} mode, the ν_{ring} mode at 1578 cm^{-1}, and the ν_{NO_2} mode at 1340 cm^{-1}, at the same excitation power density of 200 W cm^{-2}. It was apparent that the temperature elevation of the vibration modes of the molecular adsorbates were determined by both the power density of the pump laser and the spectral overlap between the molecule vibrations and the plasmon resonances. Frontiera and coworkers[140] further estimated the temperature increase under cw laser illuminations by extrapolating the temperature elevation induced by the pulsed pump laser, assuming that the heating effect had a linear dependence on incident photon flux. However, such an assumption still needs to be further validated through more careful experimental measurements and computational calculations. Because the fs-pulsed lasers incident on the samples had much higher photon flux densities than those of the cw lasers typically used for plasmon-driven photocatalysis, the photothermal heating was considered as a rather insignificant effect on the kinetic enhancement of the reactions.[140] Several other groups also claimed negligible photothermal effects on the hot electron-driven reactions under various conditions.[34–36,39,97] The accuracy in estimating the photothermal effects based on such seemingly oversimplified assumptions, however, remains questionable because the effects of collective heating, which refers to the accumulation of heat generation due to the simultaneous heating of many nanoparticles,[88,89,141–146] were not considered. Neglecting the collective heating effects may result in significant underestimate of the thermal effects, even leading to misleading conclusions for certain plasmon-driven photocatalytic reactions.[86,88,145] The heat initially generated locally at the nanoparticles diffuses into the host and establishes a steady-state temperature distribution over the photocatalyst surfaces. Although cw and pulsed illuminations may lead to very different transient heat generation and dissipation profiles, the steady-state temperature distribution is determined primarily by the averaged power absorbed by the nanoparticles, regardless of whether the excitation patterns are cw or pulsed.[145]

More recent SERS-based kinetic studies reported by several groups, however, revealed that plasmonic photothermal heating played a dominant role in the plasmon-driven photocatalytic reduction of *p*NTP under cw laser excitations,[136,147,148] which seemed to be opposite to the conclusions drawn by Frontiera and coworkers.[140] As shown in Fig. 9D, under the excitations by a 785 nm cw laser, no spectral features of DMAB was observed in either Stokes or anti-Stokes SERS spectra at low excitation power densities, whereas at high excitation power densities, the DMAB peaks were clearly resolvable and became particularly prominent in the anti-Stokes SERS spectra.[147] Based on the relative intensities of the vibrational modes in the Stokes and anti-Stokes spectra, the temperature increase of the DMAB vibrations was calculated to be around 350 K at an excitation power density of 127 kW cm^{-2}. The significant increase in the vibrational temperatures of the molecular adsorbates kinetically boosted the plasmon-driven reactions, which was verified by the time-resolved SERS results at various controlled bath temperatures (Fig. 9E and F). The reaction rates of the *p*NTP coupling at various temperatures followed the Arrhenius equation (Fig. 9G), which indicated that the reaction rates were predominantly influenced by the local temperature at the photocatalyst surfaces. However, without laser illumination, no DMAB was produced even at temperatures as high as 175 °C, indicating that this reaction could not be thermally activated without plasmon excitations. Combining all the evidences, it could be concluded that the reductive coupling of *p*NTP was essentially a photocatalytic reaction driven by the energetic hot carriers, while the elevated local temperature experienced by the molecules could further enhance the reaction kinetics.

3.3 Plasmon-driven decarboxylation of mercaptobenzoic acid (MBA)

The photo-excited plasmonic hot carriers can be harnessed not only to drive the bond-forming molecular coupling reactions, such as the oxidative coupling of *p*ATP and reductive coupling of *p*NTP, but also to develop optical molecular scissors for site-selective bond cleavage in molecular adsorbates, as exemplified by the plasmon-driven decarboxylation of MBA adsorbed on nanostructured Au and Ag surfaces. In the large family of carboxylic acid molecules, 1,3-diacids readily undergo decarboxylation reactions under thermal conditions at elevated temperatures,[149] whereas the efficient decarboxylation of aromatic monocarboxylic acids requires much harsher reaction conditions and relies critically on the use of specifically designed catalysts.[150] In addition, the yield of the decarboxylated products typically remains rather low unless electron-withdrawing functional groups are introduced to the *ortho*-positions on the aromatic rings.[151] Plasmon-driven photocatalysis constitutes a unique light-triggered approach to the efficient decarboxylation of aromatic carboxylic acids under mild reaction conditions.

The decarboxylation of surface-adsorbed MBA during SERS measurements was first observed by Michota and Bukowska in 2003.[152] When using SERS to monitor the self-assembly of MBA on the surfaces of Au and Ag electrodes, they observed the emergence of three new Raman bands at 689, 998, and 1020 cm^{-1} in addition to all the characteristic peaks of MBA. These newly emerging peaks were all characteristic Raman features of mono-substituted benzene derivatives, signifying the formation of thiophenol derived from the decarboxylation of surface-adsorbed MBA. Without recognizing the underlying critical roles of the plasmon resonances of the metal substrates, they claimed that the decarboxylation

reaction was triggered by the nanoscale roughness on the metal surfaces, because the SERS spectral features of MBA on smooth Ag and Au surfaces remained essentially unchanged and none of the characteristic thiophenol peaks was developed in the SERS spectra throughout the entire molecular self-assembly processes. Such a decarboxylation reaction occurred only in neutral and basic reaction media, whereas it became unobservable in acidic environments, further suggesting that the decarboxylation of MBA molecules was triggered by the interactions of the deprotonated carboxylate group (COO^-) with the metal surfaces. The emergence of the Raman signatures of the mono-substituted benzene rings in the SERS spectra of MBA has also been alternatively interpreted as a direct consequence of chemical enhancement arising from interfacial charge transfer. Zhao and coworkers[153] observed strong SERS peaks of the in-plane ring breathing modes of mono-substituted benzene at 998 and 1020 cm^{-1} when aniline formed intermolecular H bonds with the MBA molecules adsorbed on Ag nanoparticle surfaces. They argued that instead of being the Raman signatures of thiophenol, the SERS peaks at 998 and 1020 cm^{-1} should be assigned to the non-totally symmetric (b_2) modes of MBA, which were selectively enhanced hypothetically by the charge-transfer transitions from the Fermi level of the Ag nanoparticles to the LUMO of the surface-adsorbed MBA promoted by intermolecular H-bonding between MBA and aniline. At first glance, both the surface roughness and the charge transfer effects seemed reasonable for interpreting certain aspects of the SERS features of the surface-adsorbed MBA molecules. However, closer scrutiny of more detailed kinetic results obtained from deliberately designed *in situ* SERS measurements pointed to a more convincing mechanistic picture that fully captured the essence underpinning the SERS spectral evolution. In 2013, Yao and coworkers[154] pointed out that the previously observed temporal evolution of the SERS spectral features of MBA signified the transformation of MBA into thiophenol through decarboxylation, which was essentially a unique plasmon-driven molecule-transforming process occurring in the plasmonic hot spots.

Yoon and coworkers[155] carried out systematic SERS studies of the decarboxylation reaction of MBA molecules located in gap-mode plasmonic hot spots at various excitation wavelengths and pH values, which provided compelling experimental evidence on the curial roles that plasmonic hot carriers played in driving the decarboxylation reactions. As illustrated in Fig. 10A, a nanoparticle-on-mirror (NPoM) structure was assembled by placing Au nanoparticles on top of a MBA SAM-coated Au substrate. The sample was irradiated with lasers at various wavelengths to initiate the decarboxylation reactions,

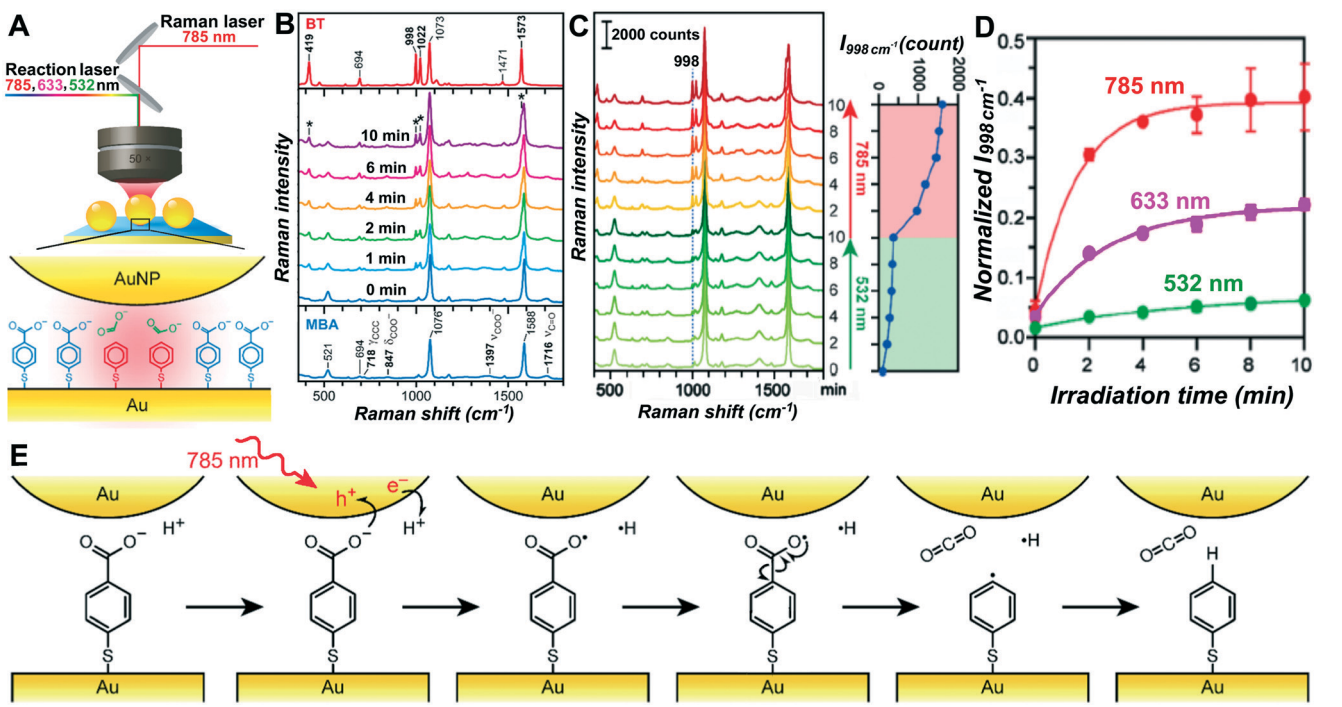

Fig. 10 (A) Scheme for studying the plasmon-driven decarboxylation of MBA. The NPoM structures were assembled by adsorbing Au nanoparticles onto MBA SAM-coated Au substrates. The reaction laser (λ = 785, 633, or 532 nm) was focused on the NPoM structures system through a 50× objective and the reaction progress was monitored by SERS (785 nm excitation) using a Raman microscope. (B) SERS spectra at various time points during decarboxylation of MBA at 785 nm excitations. The SERS spectra of the product (thiophenol) and the reactant (MBA) were shown in the top and bottom of the graph, respectively. The asterisks highlight the characteristic spectral features of thiophenol. (C) The procession of thiophenol formation when the λ_{ex} was switched from 532 nm to 785 nm. The peak intensities of the 998 cm^{-1} mode were extracted and plotted. (D) Reaction kinetics at different λ_{ex}s. (E) Scheme illustrating the proposed mechanism of plasmon-driven decarboxylation of MBA sandwiched between an Au nanoparticle and an Au substrate. Reprinted with permission from ref. 155. Copyright 2019, American Chemical Society.

and the reaction progress was tracked in real time at the same spot by SERS excited at 785 nm (Fig. 10B–D). The rates of the decarboxylation reactions reached the maximum when the excitation laser was on resonance with the plasmons. As the excitation wavelength was detuned with respect to the plasmon resonance wavelength, the reaction rates dropped significantly (Fig. 10C and D). On resonance excitations of the plasmons resulted in higher abundance of hot carriers exploitable for driving the decarboxylation reaction than the off-resonance excitations. The hot carriers were generated in the Au nanoparticles through Landau damping, and subsequently transferred to the MBA molecules to induce the decarboxylation reaction, as illustrated in Fig. 10E. The hot hole acceptor was identified to be the deprotonated carboxylate anions rather than the protonated carboxylic acid, while the hot electrons were transferred to protons to produce hydrogen atoms. The hot hole injection led to the formation of a carboxyl radical intermediate, which underwent C–C bond cleavage to yield CO_2 and thiophenol. The proposed mechanism can also be seamlessly applied to interpret the hot carrier transfer processes involved in several other plasmon-driven bond cleavage reactions, such as the β-cleavage of 4-mercaptobenzyl alcohol,[155] deboronation of 4-mercaptophenylboronic acid,[156] and the C–N bond cleavage in *p*NTP.[157] It is particularly worth mentioning that only at very low surface coverage of *p*NTP, typically with only one or a few molecules in each plasmonic hot spot, could the plasmon-driven dissociation of the nitro group from surface-adsorbed *p*NTP be observed.[157] At higher *p*NTP coverage, however, the formation of DMAB through reductive bimolecular coupling of *p*NTP became kinetically favored due to the close proximity between surface-adsorbed *p*NTP molecules.[157]

In situ SERS results not only provide real time information about plasmon-driven molecular transformations, but also shed light on transient, stochastic events that are associated with plasmon-induced photophysics and photochemistry during the photoreactions. In addition to the long-term, irreversible spectral changes caused by plasmon-induced decarboxylation of MBA, individual spectral profiles emerged transiently at additional vibrational frequencies in the SERS spectra when the specific excitation power became sufficiently high.[158] Insights on the origin of these so-called individual events could be gained through cross-correlation and extreme deviation statistical analysis of the SERS intensity variations. While the evolution of the characteristic vibrational modes of the reactant and product molecules during the decarboxylation reactions could be followed through cross-correlation analysis, the transient spectral features associated with the individual events were essentially uncorrelated with each other. The occurring frequency of the uncorrelated individual events was observed to increase super-linearly with the specific excitation power, suggesting that the individual events might arise from the surface-enhanced resonant Raman scattering (SERRS) of the photothermally activated, transient local structures that were resonantly excited.[158] Although these transient events are spectroscopically resolvable by SERS, whether they can somehow dynamically maneuver the hot carrier transfer processes and to what extent they may influence the overall reaction kinetics still remain unclear and are well-worthy of more in-depth investigations.

3.4 Plasmon-mediated demethylation and decomposition of methylene blue (MB)

All the plasmon-driven photochemical reactions discussed so far in this review article are driven essentially by the interfacial transfer of hot carriers from the optically excited metallic nanostructures to either the transforming molecular adsorbates or some other charge carrier-relaying species. Besides the hot carrier-driven mechanisms, photocatalytic reactions may also occur through plasmon-enhanced intramolecular excitations without the involvement of the hot carriers. When the HOMO–LUMO energy gap of the molecular adsorbates matches the energy of plasmon resonances of the metallic nanostructures, the rate of the HOMO–LUMO interband electronic transitions in the surface-adsorbed molecules can be drastically enhanced by the photons re-radiated from the resonantly excited plasmonic nanoantennas. A prototypical reaction in this category is the plasmon-mediated *N*-demethylation of MB,[159–161] in which MB molecules adsorbed on Au nanoparticle surfaces are converted to fully demethylated thionine and other partially demethylated products, such as azure A and azure B, whose molecular structures are shown in Fig. 11A. MB and its demethylated derivatives strongly absorb light in the visible spectral region due to the HOMO–LUMO interband electronic transitions (Fig. 11B). Also shown in Fig. 11B is the light scattering spectrum of Au nanorod (~40 nm in diameter and ~90 nm in length) aggregates on a glass substrate, which displays a broad plasmon resonance band in the visible that spectrally overlaps with the absorption bands of MB and its demethylated derivatives. Habteyes and coworkers employed SERS as an *in situ* spectroscopic tool to track the plasmon-mediated *N*-demethylation of MB adsorbed on aggregated Au nanorod substrates using a 633 nm cw laser to resonantly excite both the intramolecular electronic transitions and the nanorod plasmons. Fig. 11C shows the temporally evolving SERS spectra of MB in ambient atmosphere under continuous illumination by the 633 nm laser. During the reactions, a new SERS peak emerged at 479 cm^{-1} and became progressively more intense, which could be assigned to the skeletal deformation mode of the fully demethylated product, thionine. Another new SERS peak emerged at 804 cm^{-1} was the spectral signature of the NH_2 rocking vibration of the MB-derived molecules that were completely demethylated at least at one of the N-terminals. Neither of the vibrational bands at 479 and 804 cm^{-1} were present in the SERS spectrum of MB before the reaction was initiated. The SERS peak originally at 1435 cm^{-1} was down-shifted during the reactions, which signified the formation of partially demethylated products, including both azures A and B. All

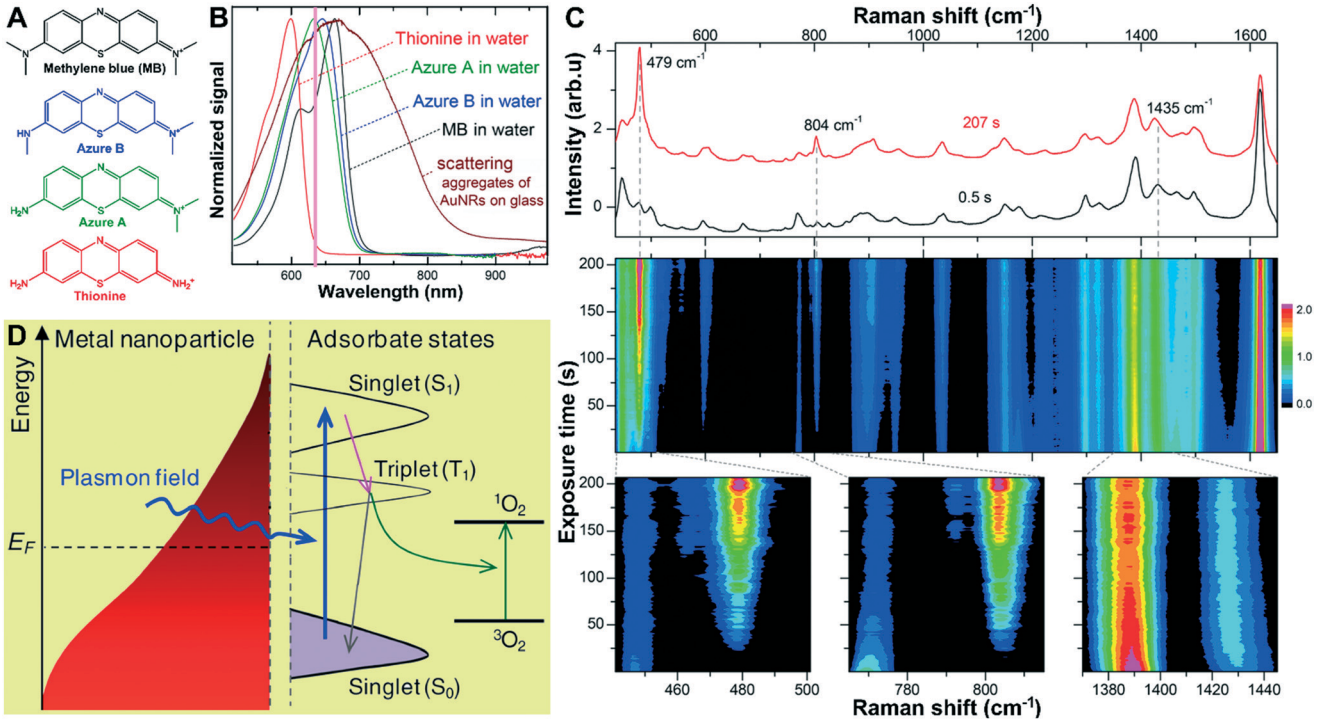

Fig. 11 (A) The molecular structures of MB, azure A, azure B, and thionine. (B) Absorption spectra of aqueous solutions of MB, azure A, azure B, and thionine and scattering spectrum of aggregated Au nanorods on a glass substrate. (C) The representative SERS spectra of MB on Au nanorod aggregates after laser illumination (633 nm) for 0.5 s and 207 s and the temporal evolution of SERS spectra during the plasmon-mediated *N*-demethylation of MB. Several zoomed-in spectral regions were shown at the bottom of the graph. (D) Schematic illustration of the plasmon-pumped intramolecular excitations that underpin the plasmon-mediated *N*-demethylation of MB. Reprinted with permission from ref. 161. Copyright 2019, American Chemical Society.

these evolving SERS spectral features could be used to track the plasmon-mediated MB demethylation process and detailed mechanistic insights were gained through a set of SERS-based kinetic measurements performed at different excitation wavelengths, in controlled reaction atmospheres, and on tunable plasmonic nanostructures.

The plasmon-mediated *N*-demethylation of MB was mechanistically distinct from those plasmonic hot carrier-driven reactions, as manifested by a unique set of intriguing characteristic phenomena.[159,160] First, the reaction rates varied significantly as the wavelengths of the excitation lasers and the plasmon resonances were systematically tuned with respect to HOMO–LUMO transition energy of the surface-adsorbed MB. The reaction proceeded at its maximal rates when the plasmon resonances of the substrates, the HOMO–LUMO interband transitions of the adsorbates, and the excitation laser were all on resonance with each other. When the excitation energy overlapped with the plasmon resonances but not with the electronic transitions of MB, almost no *N*-demethylation reaction was observed, implying that the primary driving force for demethylation reaction was the plasmon-enhanced intramolecular electronic transitions rather than the interfacial hot carrier transfer. Second, excitation of MB adsorbed on nonplasmonic surfaces at 633 nm did not lead to experimentally observable *N*-demethylation, in spite of the strong spectral overlap between the excitation laser line and the electronic transitions of MB. When adsorbed on a bulk Au film (~50 nm thick), the MB molecules well-preserved their chemical structures under continuous illumination by a 633 nm laser at power densities up to ~100 000 W cm^{-2}, whereas MB adsorbed on plasmonic Au nanostructures underwent rapid *N*-demethylation reactions at incident laser intensity as low as 100 W cm^{-2}. This observation underscored the crucial roles of the intense local fields in pumping the electronic excitation of the molecular adsorbates. Third, in ambient air and in pure oxygen atmosphere, continuous exposure of the samples to the excitation laser led to efficient *N*-demethylation of MB. However, in O_2-free inert gasses, such as an N_2 atmosphere, the conversion of MB to its demethylated products became negligible. Therefore, O_2 was indispensable in this plasmon-driven demethylation reaction. Fourth, when the surface adsorption of MB occurred in an aqueous environment, MB was most likely assembled on the Au nanoparticle surfaces in its hydrated form. The water molecules in hydrated MB served as the source of H atoms for the demethylation reactions. When MB molecules were assembled on Au surfaces in the dehydrated form (incubating MB and Au nanoparticles in ethanol solvent), the *N*-demethylation of MB was suppressed even when additional water molecules were present in the reaction atmosphere. Fifth, *N*-demethylation of MB could be further enhanced when coating the surfaces of Au nanoparticles with certain types of molecular ligands, such as a monolayer of

poly(sodium 4-styrenesulfonate). This observation suggested that introduction of a thin spacer layer between the Au surfaces and MB might optimize the surface-molecule proximity to minimize competing radiative and nonradiative processes, a unique mechanistic feature of the reactions mediated by plasmon-pumped HOMO–LUMO electronic transitions.

On the basis of all the experimental observations mentioned above, a reaction mechanism involving the participation of both O_2 and H_2O molecules has been proposed for the plasmon-mediated *N*-demethylation of MB, which is schematically illustrated in Fig. 11D.[161] Benefiting from large local field enhancements in the plasmonic hot spots, the interband electronic transitions from the singlet ground electronic state (S_0) to the singlet excited electronic state (S_1) of surface-adsorbed MB can be drastically enhanced. The excited MB molecules in the S_1 state may subsequently undergo an intersystem crossing process to populate the excited triplet state (T_1). The energy transfer from the T_1 state of MB to oxygen in its triplet ground state ($^3O_2$) leads to the generation of singlet O_2 ($^1O_2$.), a highly reactive species capable of attacking the N atoms and stripping away the methyl groups attached to N atoms. In the presence of water molecules, a radical species forms upon H-atom transfer, which leads to the *N*-demethylation and other side products. The plasmon-pumped electronic excitations of MB leads to selective dissociation of N–C bonds without causing further decomposition of the demethylated products into even smaller molecular fragments. With the aid of plasmon resonances, the S–S bond in a single $(CH_3S)_2$ molecule adsorbed on an Ag or Cu surface could also be selectively cleaved, which was recently demonstrated by Kim and coworkers through *in situ* scanning tunneling microscope (STM) studies.[162] The mechanism underpinning the plasmon-mediated S–S bond dissociation could also be interpreted in the context of plasmon-pumped direct intramolecular electronic transitions, a

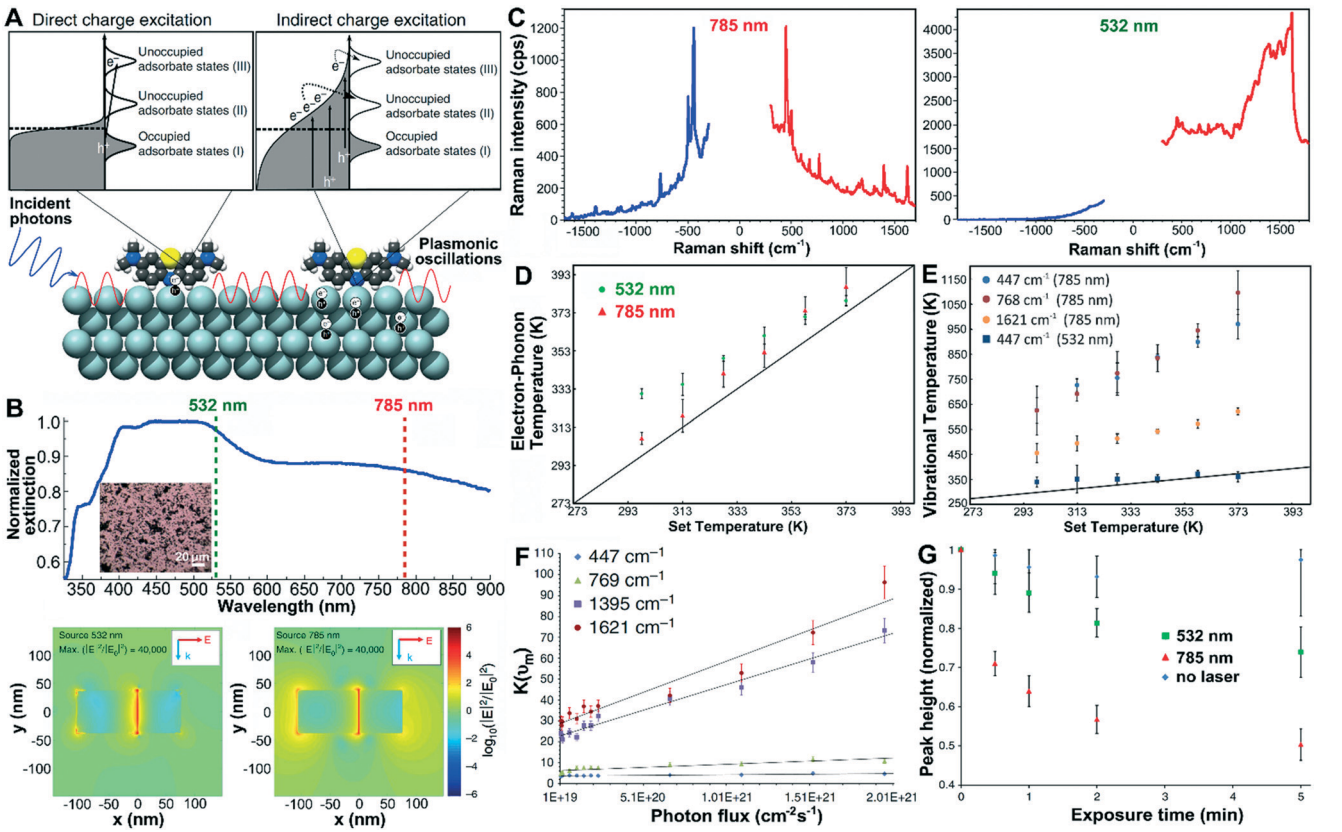

Fig. 12 (A) Scheme of two pathways for hot electrons to activate surface adsorbed molecules. Landau damping generates energetic hot electrons above Fermi level, and these hot electrons can indirectly transfer to the unoccupied orbitals of the surface adsorbates. CID can directly inject hot electrons into the unoccupied orbitals of the surface adsorbates. (B) The spectra of surface plasmon resonance of Ag nanocube aggregates deposited onto a solid substrate. The excitations are also labeled out on the spectrum. The finite-difference time domain calculated electric field enhancement of two Ag nanocubes that are 1 nm apart under 532 and 785 nm excitation are showing at the bottom of the panel. (C) The Stokes and anti-stokes spectra of MB adsorbed on Ag nanocubes with the excitation of 532 and 785 nm. (D) The temperature that the MB molecules experienced under the excitation of 532 and 785 nm laser. The error bars represent the standard deviations of all trial runs. (E) The temperature obtained based on different vibrational modes of MB on Ag nanocubes under 532 nm excitation. (F) The demonstration of excess anti-Stokes signal ratio, $K(\nu_m)$, of different MB vibrational modes at various excitation photon fluxes. The error bars represent the standard deviations obtained from three independent experiments. (G) The normalized 447 cm^{-1} peak heights of MB on Ag nanocubes at 373 K and in inert N_2 atmosphere after exposure to no laser (control, blue diamonds), 532 nm laser (green squares), or 785 nm laser (red triangles). Panels A, B, F, and G were reprinted with permission from ref. 163. Copyright 2016, Springer Nature. Panels C–E were reprinted with permission from ref. 164. Copyright 2016, American Chemical Society.

reaction pathway that did not rely on the interfacial transfer of plasmonic hot carriers.

While the plasmon-enhanced intramolecular electronic excitation has been identified as the major driving force for the selective *N*-demethylation of MB, injection of plasmonic hot carriers into the surface-adsorbed MB molecules may also occur under certain photoexcitation conditions, which leads to further fragmentation or decomposition of the surface-adsorbed MB molecules.[163] As illustrated in Fig. 12A, the plasmon hot carriers may get injected into the molecular adsorbates either through indirect charge transfer following Landau damping or through CID, which involves direct excitation of an electron into an unoccupied orbital of the molecular adsorbate that are strongly coupled with the metallic nanoparticles. Because the direct and indirect charge injection mechanisms are featured by drastically different energy profiles of hot electrons, it is of pivotal importance to develop solid understanding of their relative contribution to plasmon-induced photocatalytic reactions. Plasmon-induced decomposition of MB adsorbed on Ag nanoparticle surfaces constitute a representative model reaction ideal for such mechanistic investigations.

Linic and coworkers[163] discovered that MB molecules adsorbed on Ag nanocube aggregates underwent photo-induced decomposition through a direct charge excitation mechanism at 785 nm excitations. The Ag nanocube aggregates exhibited broad plasmon resonance bands spanning the visible and near-infrared spectral regions (Fig. 12B) due to the strong plasmon coupling between neighboring nanocubes. The local electric fields in the junctions between adjacent nanocubes were drastically enhanced upon plasmonic excitations at both 532 and 785 nm (Fig. 12B), providing hot spots for SERS. Although the intensity ratios of anti-Stokes *vs.* Stokes peaks in the SERS spectra were close to the expected values at certain temperatures at 532 nm excitations, the anti-Stokes peaks became drastically stronger than expected at 785 nm excitations (Fig. 12D), which could not be interpreted solely as the results of local photothermal heating in the plasmonic hot spots. The electron–phonon temperatures (equilibrated local temperatures at nanoparticle surfaces) and the vibrational temperatures of specific Raman modes could be evaluated by analyzing the anti-Stokes and Stokes SERS spectral features.[164] The anti-Stokes background intensity was related to the local equilibrated temperature of the metal through the following equation derived from the Fermi–Dirac distribution function

$$I_{\mathrm{aS,background}} = \frac{I_{\mathrm{aS},0}}{e^{E_{\mathrm{Raman}}/k_{\mathrm{B}}T} + 1},$$

where $I_{\mathrm{aS,background}}$ was the background intensity of the anti-Stokes SERS at a given energy of Raman shift, E_{Raman}, and $I_{\mathrm{aS},0}$ was the anti-Stokes intensity at E_{Raman} of 0. Assuming that the thermalized vibrational energy distribution obeyed the Boltzmann distribution, the effective vibrational temperatures of a specific Raman mode of the molecular adsorbents could be calculated using the following equation

$$T_{\mathrm{vibr}} = -\frac{E_{\mathrm{vibr}}}{k_{\mathrm{B}} \ln(I_{\mathrm{aS}}/I_{\mathrm{St}})},$$

where E_{vibr} was the energy of the vibrational mode, and I_{aS} and I_{St} were the intensities of anti-Stokes and Stokes peaks in the SERS spectra, respectively. As shown in Fig. 12D, for both excitation wavelengths, the local nanoparticle temperature under laser illumination was slightly above the bulk temperature in the reactors due to the plasmonic photothermal heating effect. At the same excitation power densities, 532 nm excitation resulted in higher temperature elevation of the nanoparticles than the 785 nm excitation because of higher photon energy of the 532 nm laser. Interestingly, with a photon flux of 2.0×10^{20} photons cm^{-2} s^{-1} incident on the sample, the vibrational temperatures of the Raman modes of MB were dramatically elevated compared to local nanoparticle temperature at the 785 nm excitations, whereas under illumination by the 532 nm laser, the local nanoparticle temperatures and the vibrational temperatures appeared very similar to each other (Fig. 12E).

The degree by which the SERS anti-Stokes signal of a specific vibrational mode exceeded the expectation according to the Boltzmann distribution, $K(\nu_{\mathrm{m}})$, was defined using the following equation:[163]

$$K(\nu_{\mathrm{m}}) = -\frac{I_{\mathrm{aS}}^{\mathrm{SERS}}(\nu_{\mathrm{m}})/I_{\mathrm{St}}^{\mathrm{SERS}}(\nu_{\mathrm{m}})}{I_{\mathrm{aS}}^{\mathrm{tol}}(\nu_{\mathrm{m}})/I_{\mathrm{St}}^{\mathrm{tol}}(\nu_{\mathrm{m}})},$$

where $I_{\mathrm{aS}}^{\mathrm{SERS}}(\nu_{\mathrm{m}})$ and $I_{\mathrm{St}}^{\mathrm{SERS}}(\nu_{\mathrm{m}})$ represented the anti-Stokes and Stokes peak intensities of a vibrational mode, ν_{m}, in the SERS spectra of MB adsorbed on Ag surfaces. $I_{\mathrm{aS}}^{\mathrm{tol}}(\nu_{\mathrm{m}})$ and $I_{\mathrm{St}}^{\mathrm{tol}}(\nu_{\mathrm{m}})$ were the anti-Stokes and Stokes intensities of similar vibrational modes in the normal Raman spectra of liquid toluene, which served as an internal reference system obeying the Boltzmann distribution. Linic and coworkers associated the large deviation between the equilibrated temperatures of nanoparticles and the vibrational temperatures of MB molecules at 785 nm excitations with the direct charge excitations in the Ag–MB complex system at this particular excitation wavelength. The linear relationship between the $K(\nu_{\mathrm{m}})$ values and the incident photon flux (Fig. 12F) for all the analyzed vibrational modes also indicated an optically pumped direct charge transfer mechanism in the hybrid MB–Ag complex system at 785 nm excitations. The direct charge transfer through CID at 785 nm excitations resulted in rapid decomposition of the surface-adsorbed MB molecules, which was evidenced by the fast decay in SERS signals over time (Fig. 12G).

The effects of direct charge excitations in the Ag–MB complex system claimed by Linic and coworkers, however, are still open to further scrutiny. The accuracy of Raman thermometry based on Stokes/anti-Stokes ratios may deteriorate significantly when electronic transitions and plasmons are resonantly excited, an effect not further

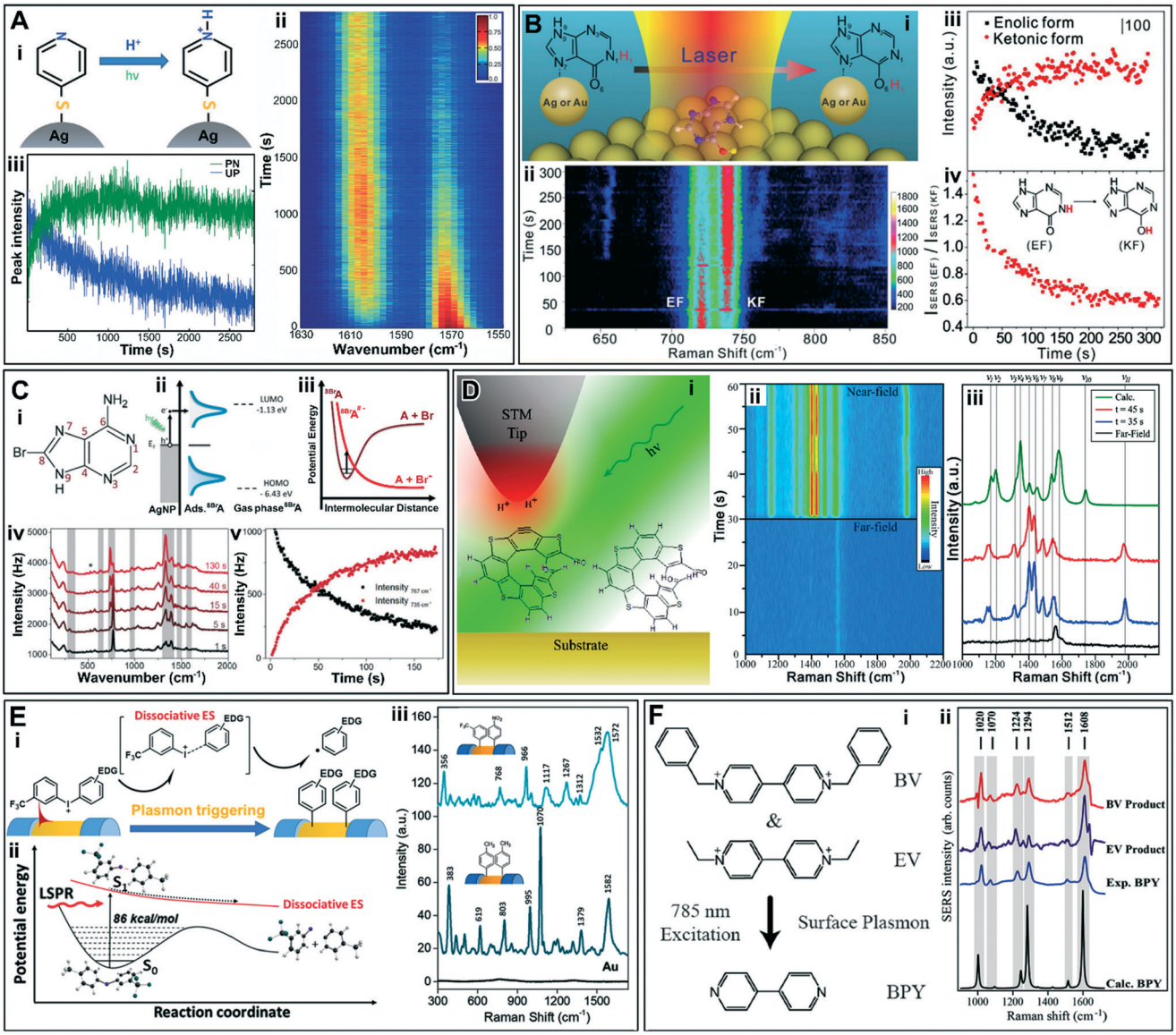

Fig. 13 (A) Plasmon-driven protonation of 4-MPY: (i) schematic illustration of protonation of 4-MPY adsorbed on Ag nanoparticle surfaces; (ii and iii) time-resolved SERS spectra highlighting the transition from the unprotonated to the protonated form. The Raman peaks at 1575 and 1608 cm^{-1} corresponded to the ring breathing modes of the unprotonated and the protonated form of 4-MPY, respectively. Reprinted with permission from ref. 174. Copyright 2014, the Royal Society of Chemistry. (B) Plasmon-driven intramolecular proton transfer of hypoxanthine: (i) schematic illustration of the reaction; (ii) time-resolved SERS spectra showing the transition from the enolic form (EF) to the ketonic form (KF) of hypoxanthine adsorbed on plasmonic Au nanoparticle at 633 nm excitations; (iii) the temporal evolution of the SERS peak intensities at 724 (KF) and 744 cm^{-1} (EF); (iv) the conversion of EF to KF. Reprinted with permission from ref. 175. Copyright 2017, the Royal Society of Chemistry. (C) Plasmon-driven C–Br bond cleavage of 8-bromoadenine: (i) molecular structure of 8-bromoadenine; (ii) scheme illustrating the transfer of hot electrons into the LUMO of 8-bromoadenine adsorbed on Ag nanoparticle surfaces; (iii) schematic potential energy diagram illustrating the C–Br bond dissociation of the molecule in its excited electronic state; (iv) SERS spectra at various reaction times and (v) temporal evolution of C–Br bond cleavage of 8-bromoadenine induced by surface plasmon. Reprinted with permission from ref. 176. Copyright 2017, the Royal Society of Chemistry. (D) Plasmon-induced dehydrogenation of 2,13-bis(aldehyde)-[7]thiaheterohelicene: (i) schematic demonstration of dehydrogenation induced by green laser (532 nm) excited surface plasmons; (ii) temporal evolution of the far-field (0–30 s) and near-field spectra (31–60 s); (iii) the comparison of the near-field spectra at time points of 35 and 45 s, the averaged far-field spectrum and DFT calculated Raman spectrum. Reprinted with permission from ref. 177. Copyright 2017, American Chemical Society. (E) Plasmon-mediated C–I bond cleavage in unsymmetric iodonium salts: (i) schematic illustration of the proposed reaction mechanism; (ii) schematic illustrate of the C–I bond cleavage triggered by plasmon-enhanced intramolecular electronic excitations; (iii) SERS spectra of two unsymmetric iodonium salts after the photoreactions. The compound at the bottom showed regioselectivity in reactions, whereas the one at the top did not show such regioselectivity. Reprinted with permission from ref. 178. Copyright 2020, American Chemical Society. (F) Plasmon induced C–N bond cleavage in viologen derivatives: (i) molecular structures of benzyl viologen (BV), ethyl viologen (EV), and 4,4′-bipyridine (BPY); (ii) SERS spectra of BV, EV, and BPY, and DFT-calculated Raman spectra of BPY. Reprinted with permission from ref. 179. Copyright 2019, American Chemical Society.

considered in Linic's work. The origin of the spectral background in the Stokes and anti-Stokes SERS spectra, which is typically described as luminescence from the plasmonic nanostructures, is mechanistically complex. The mechanisms for luminescence from optically excited Au and Ag nanostructures have been interpreted in the context of either radiative recombination of hot carriers (photoluminescence)[165–167] or electronic Raman scattering (inelastic light scattering).[168,169] Link and coworkers[170] recently showed that analysis of the Stokes/anti-Stokes emission intensity ratios yielded temperatures that could only be interpreted as originating from the excited electron distribution and not a thermally equilibrated phonon population. Therefore, the accuracy of calculating the equilibrated electron–phonon temperatures based on the continuum background in SERS spectra still needs to be further tested. With recent advances in fundamental understanding and methodology development of nanothermometry and thermoplasmonics,[85–87,171–173] more accurate measurements of the local temperature at nanoparticle surfaces under light illumination become possible, which will allow us to carefully revisit previous conclusions drawn from the Raman thermometry and better quantify the thermal and nonthermal effects on plasmon-driven reactions.

3.5 Other recently discovered plasmon-driven photocatalytic reactions

Insights gained from the detailed case studies of several representative reactions discussed in the previous sections in this review provide a solid knowledge foundation for mechanistic understanding of plasmon-driven photocatalysis. Over the past few years, numerous new reactions have been discovered and added to the continuously expanding library of plasmon-driven photocatalytic reactions. Here we present a brief survey of several newly discovered plasmon-driven reactions, during which the detailed structural evolution of the transforming molecules can be monitored *in situ* by SERS or TERS. Singh and Deckert[174] discovered that 4-mercaptopyridine (4-MPY) adsorbed on Ag nanoparticle surfaces became protonated in ambient air when irradiated by 532 nm laser (Fig. 13A). Liu and coworkers[175] observed that surface-adsorbed hypoxanthine molecules underwent a unique plasmon-driven intramolecular proton transfer process, in which the enolic form was converted to the ketonic form (Fig. 13B). Schürmann and Bald[176] found that the hot electron injection into the LUMO of surface-adsorbed 8-bromoadenine led to the selective dissociation of the C–Br bond (Fig. 13C). Chaunchaiyakul and coworkers[177] demonstrated that a Ag tip could act as both a local heat source and a plasmonic catalyst to induce dehydrogenation reactions on one of the benzene rings of 2,13-bis(aldehyde)-[7]thiaheterohelicene, though which a C≡C bond was created at the location in close proximity to the tip (Fig. 13D). Postnikov and coworkers[178] observed that plasmon resonances could effectively induce the site-selective cleavage of the C–I bond in unsymmetrical iodonium salts and the formation of electron-rich radical species (Fig. 13E). The high regioselectivity of the bond cleavage essentially originated from the plasmon-pumped electronic excitations from the ground state to a dissociative excited state. Frontiera and coworkers[179] found that localized plasmon resonances could be harnessed to trigger the C–N bond cleavage across a series of viologen derivatives, such as benzyl viologen (BV) and ethyl viologen (EV), through which a photo-stable final product, 4,4′-bipyridine (BPY), was produced (Fig. 13F). It was hypothesized that the hot electron injection into surface-adsorbed O_2 resulted in the formation of anionic O_2^-, which acted as a reactive intermediates triggering the C–N bond cleavage. Although more detailed mechanistic investigations are still underway, the mechanisms of these recently discovered reactions can all be interpreted in the broad context of surface photochemistry driven by either plasmonic hot carriers or plasmon-enhanced intramolecular electronic excitations, possibly entangled with additional kinetic enhancement caused by local photothermal heating at the photocatalyst surfaces.

4. Plasmonic hot electron-driven photocatalysis *versus* secondary electron-induced surface chemistry

Our understanding of plasmon-driven photocatalysis has been progressing primarily in an empirical, discovery-driven fashion, typically initiated by discovery of new reactions, followed by systematic kinetic studies under controlled reaction conditions, and in some cases further corroborated by computational simulations, based upon which plausible reaction mechanisms can be eventually proposed and further tested. However, it remains an extremely challenging task to rationally predict the reaction outcomes and pathways of a previously unexplored nanostructure-adsorbate system under a given set of photoexcitation and reaction conditions. Because of the fundamental differences in the mechanisms of the plasmon-driven photocatalysis and the thermally activated surface chemistry, there is limited information one can extract from the large body of the literature on heterogeneous catalysis to develop predictive tools for the plasmon-driven photocatalytic molecular transformations. A particularly enlightening discovery recently made by Zenobi and coworkers,[180] which draws the connection between the plasmon-driven photocatalysis and the surface chemistry induced by X-ray and electron beam irradiation, represents an important step toward filling this knowledge gap. Through combined TERS, SERS, and temperature programmed desorption mass spectrometry (TPD-MS) measurements, Zenobi and coworkers[180] found that the products of plasmon-driven photocatalytic reactions were similar to the those produced from the X-ray and electron beam-induced surface reactions on planar metallic surfaces, which have

been relatively well-studied by the surface chemistry community. The plasmon-driven photocatalytic reactions occurred among the molecules residing in the gap-mode electromagnetic hot spots, which could be created by either densely packing metallic nanoparticles on a substrate (Fig. 14A) or bringing a metal tip in close proximity to a metallic substrate (Fig. 14B). The plasmon-driven molecular transformations in these two types of hot spots could be tracked in real time using SERS and TERS, respectively. Although the energies of X-ray and electron beams are about two orders of magnitude higher than those of the visible or near-infrared photons commonly used for plasmon-driven reactions, irradiation of the molecular adsorbates on metallic substrates with X-ray or electrons may result in surface molecular transformations surprisingly analogous to those driven by plasmonic hot electrons. It is essentially the lower-energy secondary electrons scattered off the metal surfaces rather than the higher-energy primary particles in the incident X-ray or electron beams that induces the interfacial molecular transformations (Fig. 14C). In contrast to the hot electron-driven reactions that are locally confined within the plasmonic hot spots, the secondary electron-induced surface reactions may happen uniformly over the entire electron beam- or X-ray-irradiated substrate surfaces.

Fig. 14D and E show the TERS spectra reflecting the chemical transformations of 1-hexadecanethiol (HDT) and biphenyl-4-thiol (BPT) SAMs sandwiched between a TERS tip and an Au substrate under excitation by a 633 nm laser at various excitation powers. Both HDT and BPT underwent interesting plasmon-driven transformations involving a series of bond-forming and bond-breaking processes, as evidenced by the changes in their TERS spectral features. For HDT, the emergence of TERS peaks at 980, 1580 and, 2110 cm^{-1} signified the formation of S–O bond, the C═C bond, and C≡C bond, respectively. The formation of these new bonds in the HDT SMAs was accompanied by the cleavage of some other chemical bonds originally existed in the pristine SAMs, such as the C–S and C–C bonds. In the case of BPT, the

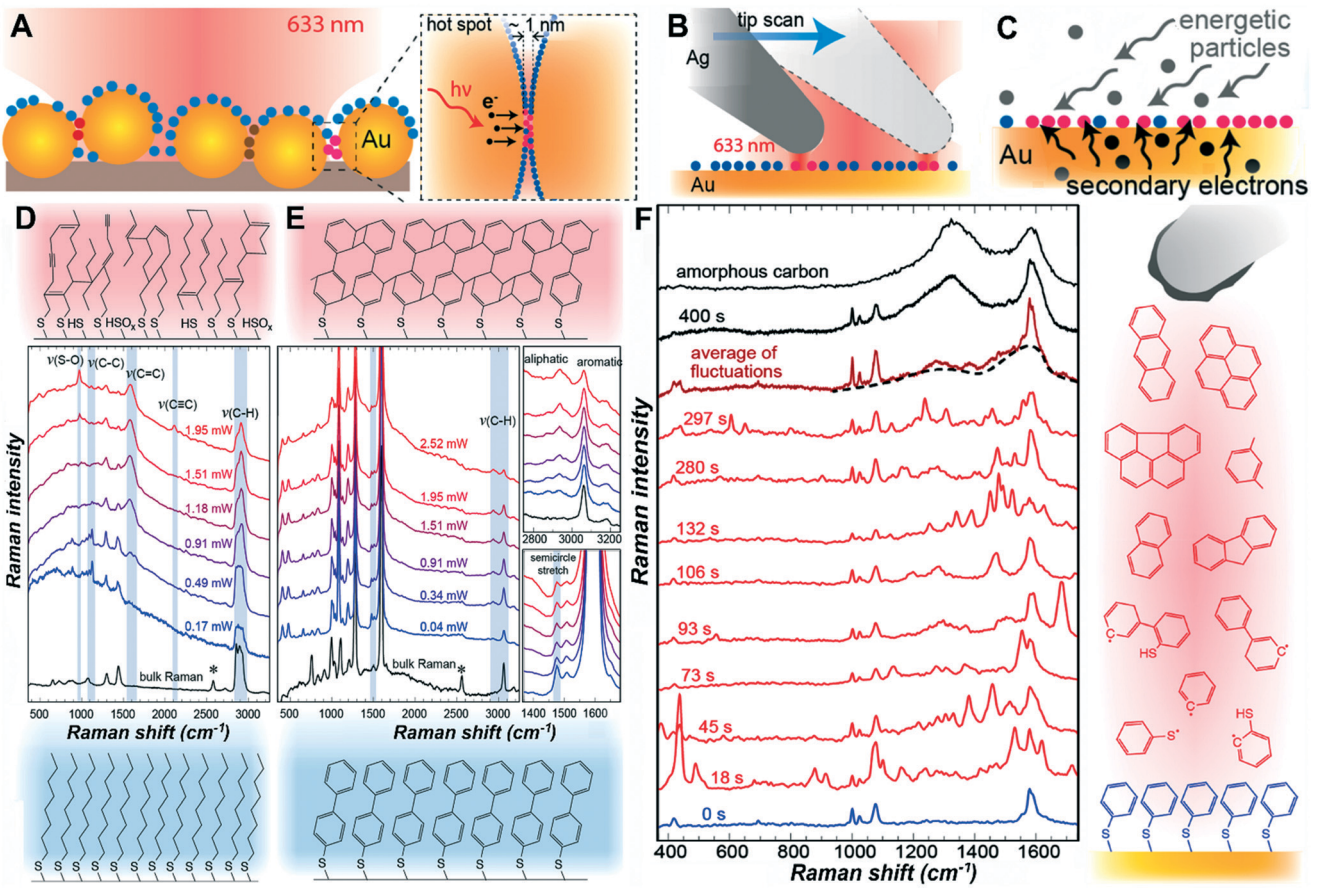

Fig. 14 Schematic illustration of photocatalytic reactions in plasmonic hot spots located (A) within inter-nanoparticle junctions and (B) a tip-substrate junction. (C) Schematic illustration of surface reactions induced by the secondary electrons when the Au surface is bombarded by energetic particles, such as X-ray photons or low energy electrons (<50 eV). TERS spectra showing the plasmon-induced transformations of (D) HDT and (E) BPT SAMs on Au surfaces. The pristine SAM structures and the product molecules after the plasmon-driven transformations are shown in the lower and upper parts of TERS spectra, respectively, in panels D and E. (F) The snapshot SERS spectra showing the structural evolution of thiophenol SAMs on Au surfaces during plasmon-driven transformations. The spectral fluctuations in the spectral range of 1200–1700 cm^{-1} indicated the formation of a variety of polycyclic aromatic hydrocarbons (PAHs). The possible structures of these PAHs are shown in the right panel next to the spectra. Reprinted with permission from ref. 180. Copyright 2018, American Chemical Society.

intensity evolution of the semicircle stretching (1485 cm^{-1}) peak of benzene and the C–H stretching modes were indicative of the cross-linking of benzyl rings. These products formed through the plasmon-driven photocatalytic reactions were very similar to the those obtained by bombarding low energy electrons (<50 eV) at the same molecules adsorbed on Au surfaces.[181,182] Both TPD-MS and anti-Stokes TERS results strongly suggested that these molecular transformations were essentially driven by the plasmonic hot carriers rather than being thermally induced.

Besides the desired products, side products may also be produced during the plasmon-driven reactions. In numerous cases, photo-induced damage of molecules in the hot spots, sometimes also referred to as sample burning, may occur during SERS and TERS measurements at high excitation power densities due to the formation of amorphous carbon on the nanostructure surfaces. The amorphous carbon may also form on the catalyst surfaces through thermal catalytic conversions, which typically leads to the deactivation of the catalysts. The TERS results in Fig. 14F clearly show the formation of amorphous carbon ($(CH_x)_n$, $0.2 \leq x \leq 1.0$) through plasmon-induced photocatalytic transformations of a self-assembled thiophenol monolayer on an Au substrate. Upon prolonged laser irradiation, parasitic spectral features emerged in the TERS spectra, with temporally fluctuating peaks appearing at random positions, mostly between 1200 and 1700 cm^{-1}. These fluctuating peaks could be assigned as the spectral features of various transient intermediates, presumably polycyclic aromatic hydrocarbons (PAHs), generated during the sample degradation process. Spectral average over these fluctuating peaks gave rise to two broad background humps, which well-resembled the spectral features of the amorphous carbon. The fluctuating spectral features of the transient intermediates observed in TERS and SERS, in numerous cases, were misinterpreted as the signatures of single-molecule events or structurally dynamic biomolecules.[47,57–62] The conversion of surface-adsorbed organic SAMs into amorphous carbon observed in TERS is essentially a plasmon-driven analog to the sample carbonization processes induced by X-ray and electron beams. Carbonization of sample surfaces is a well-known phenomenon in scanning electron microscopy (SEM) and X-ray photoelectron spectroscopy. When exposed to the scanning electron beam, amorphous carbon can be built up on the sample surfaces due to the carbonization of the molecular adsorbates on the sample surfaces driven by the secondary electrons scattered off the substrate. Similar carbonization processes may also occur during XPS measurements. It is worth mentioning that the mechanism of sample carbonization through plasmon-driven photocatalysis is fundamentally different from the pyrolysis or combustion processes occurring under thermal conditions, which do not involve any hot carriers or secondary electrons.

The remarkable analogy between the plasmon-driven photocatalysis and the surface chemistry induced by X-ray/electron-beam irradiation coincides with the similarity in electron energies for the secondary electrons and plasmonic hot electrons. Within this context, the plasmon-driven photocatalysis can be considered as a member in a much larger family of charge carrier-mediated surface chemistry. Many reactions known from the surface science literature, including those induced by electron beams, X-ray, and femtosecond laser pulses in ultrahigh vacuum conditions, may also occur on plasmonic nanostructured surfaces through hot carrier-mediated pathways to produce similar products.

5. Concluding remarks

Plasmon-driven photocatalysis has emerged as a paradigm-shifting approach capable of regioselectively tailoring the structures and properties of the molecular adsorbates residing in the plasmonic hot spots on nanostructured metal surfaces. Enlightened by the thought-provoking insights gained from deliberately designed *in situ* plasmon-enhanced Raman spectroscopic measurements over the past decade, a unified mechanistic picture has started to emerge, which creates a generic knowledge framework for interpreting the complex mechanisms underpinning a broad scope of plasmon-driven reactions. Despite their remarkable diversity, the plasmon-mediated photocatalytic reactions can be classified into four broadly defined categories, according to which plasmon decay pathway dominates the reaction mechanism. Because each type of reactions has its own unique mechanistic and kinetic characteristics, different design principles should be taken into considerations accordingly to rationally guide the structural optimization of both the plasmonic photocatalysts and the molecular adsorbates for specific types of plasmon-mediated molecule-transforming processes.

The type-I reactions are essentially driven by the hot carriers, in most cases the energetic hot electrons, generated through the Landau damping. The kinetics and efficiencies of the type-I reactions are determined by several key factors, such as the energy distribution of the hot electrons, the life time of the hot electrons, and the energy alignment of the unoccupied molecular orbitals with respect to the Fermi level of the metallic nanostructures. The transient energy distribution of the nonthermal hot carriers immediately after the photo-excitations depends on the energies of the excitation photons that are on resonances with the plasmons. The hot carrier-driven photocatalytic reactions typically exhibit rather low quantum efficiencies, which are intrinsically limited by the short life-times of the hot carriers. The life times of the hot carriers can be tuned within a certain range by changing the size, shape, and composition of the plasmonic nanostructures. Electrodynamic simulations serve as valuable computational tools that can aid in the design of the materials. An alternative way to increase the life-times of the hot carriers is to place electron-accepting or electron-donating species, either molecules or semiconductors, in direct contact with the plasmonic nanostructures to promote the charge separations. Because of carrier relaxation that occurs rapidly after photoexcitation

of the hot carriers, close energy match between an unoccupied molecular orbital and the Fermi level of the metal is highly desirable for efficient injection of the hot electrons into the molecular adsorbates.

The type-II reactions are driven by direct excitation of electrons in an adsorbate orbital through CID. CID occurs upon efficient photoexcitation of certain electronic transitions between the hybrid orbitals of strongly coupled nanostructure-adsorbate systems that are on resonance with the excitation photons. Identifying these resonance modes in nanostructure-adsorbate hybrid systems is not an easy task and DFT calculations can be used as a computational tool to help predict and understand the formation of hybrid orbitals in these strongly coupled systems. More in-depth mechanistic investigations are still needed to fully elucidate the energy landscapes and kinetic profiles associated with the CID-mediated photocatalytic reactions.

The type-III reactions are driven by the plasmon-enhanced intramolecular electronic excitations, a mechanism that does not involve the injection of hot carriers into the molecular adsorbates. The efficiency and rates of this type of reactions are profoundly influenced by the local-field enhancements and the spectral overlap between the plasmon resonances and the HOMO–LUMO interband transitions. Taking full advantage of the plasmonic tunability offered by metallic nanostructures, the plasmon resonance frequencies can be systematically tuned with respect to the HONO–LUMO band gap of the adsorbates to meet the requirement for on-resonance excitations. The amplitude of the local plasmonic fields are sensitively dependent upon the structures of the plasmonic photocatalysts and the distance between the molecular adsorbates and the metal surfaces. The dependence of reaction rates on the local fields, however, may vary drastically from reaction to reaction, depending on the detailed mechanisms involved in the molecule-transforming processes.

The type-IV reactions are those kinetically enhanced by plasmonic photothermal heating, such as the Suzuki coupling reaction catalyzed by Pd-coated Au nanoparticles.[183] These reactions can also take place under thermal conditions, and their fundamental mechanisms are not altered by the plasmon resonances of the metallic nanocatalysts. However, the reaction rates can be greatly enhanced purely due to the elevation of the local temperature on the photocatalyst surfaces under light illumination. This type of reactions should be more accurately termed as plasmon-enhanced catalytic reactions rather than plasmon-driven photocatalytic reactions. Because their mechanisms remain essentially the same as those of the thermal catalytic reactions, we decided not to present more detailed discussions on this type of reactions in this review article.

Finally, we wrap up our discussions by pointing out several relatively unexplored directions that are well-worthy of further investigations and scrutiny in the future.

(1) In addition to the plasmonic excitations within the conduction band of the metals, hot carriers can also be generated in the metallic nanostructures upon the optical excitations of the d-to-sp interband transitions.[184] It has been demonstrated by several case studies that the interband hot carriers can be photocatalytically more efficient than the plasmonic intraband hot carriers in driving certain reactions.[185–189] The interband hot electrons may also couple with the plasmonic electron oscillations to give rise to new plasmon resonance modes in the metallic nanostructures,[190] potentially creating additional pathways for the hot carrier transfer in nanostructure-adsorbate systems. While the plasmonic intraband excitations primarily produce energetic electrons exploitable for photocatalysis, the interband excitations of metallic nanostructures leads to highly energetic hot holes well below the Fermi level of the metal. How these interband hot holes behave differently from the plasmonic hot electrons when executing their photocatalytic functions represents a fundamentally intriguing question.

(2) The plasmon-driven reactions discussed in this review all occur locally in the plasmonic hot spots, which provides a unique means of tailoring the surface chemistry of metallic nanostructures within nanoscale confinement. However, it remains challenging to scale up the reactions, which limits the potential of developing plasmon-driven photocatalysis into a scalable synthetic tool for real-world applications. For the application-oriented purpose, there is an urgent need to design and engineer the catalyst and the reactor configurations that allow us to efficiently harvest the sun light to drive plasmon-driven reactions on a larger scale.

(3) The use of plasmon-driven photocatalysis to tailor the surface chemistry of metallic nanoparticles for biomedical applications needs to be further demonstrated. As exampled by multiple reactions discussed in this review, the plasmon resonances can induce selective bond cleavage in the molecular adsorbates. Therefore, plasmon-triggered drug delivery systems can be developed by selectively conjugating desired molecular moieties to the plasmonic hot spots on the nanoparticle surfaces. By tuning the plasmon resonances of the nanoparticles to the near-infrared water windows, it becomes possible to use deep-penetrating near-infrared light sources to trigger targeted drug release from plasmonic nanocarriers in living systems.

(4) The research on plasmon-mediated surface chemistry has been focusing on nanostructures composed of noble metals so far. However, the high cost and scarcity of these noble metal elements inevitably limits their large-scale applications in catalysis, optoelectronics, and biomedicine. A variety of alternative materials,[191–193] which are cheaper and more earth-abundant than the noble metals, also exhibit interesting plasmonic properties potentially exploitable for plasmon-driven photocatalysis. These materials include non-noble metals, such as Al[194–196] and Mg,[197] and degenerately doped semiconductors, such as non-stoichiometric copper chalcogenides and doped oxides.[198–207] Although largely unexplored, plasmon-mediated surface chemistry on these alternative plasmonic materials represent a research area that is fundamentally interesting and potentially transformative.

The success in using these non-noble metal materials as the plasmonic photocatalysts may not only further expand the scope of the plasmon-mediated surface chemistry, but also effectively mitigate the cost issues associated with the noble metal-based plasmonic photocatalysts for real-world applications.

Plasmon-mediated surface chemistry has been an emerging area full of open questions, opportunities, and challenges. The research on plasmon-driven photocatalysis has reached a critical stage, at which some important conclusions drawn from earlier studies concerning the detailed reaction mechanisms become well-worthy of careful reexamination and need to be refreshed with new perspectives. With its unique structure-resolving capability and ultrahigh surface sensitivity, plasmon-enhanced Raman spectroscopy has become an extremely powerful tool fueling new discoveries and in-depth mechanistic explorations in the field of plasmon-mediated surface chemistry. The mechanistic insights extracted from the *in situ* SERS and TERS results provide central guiding principles for the development of next generation plasmonic photocatalysts. Pushing the mechanistic understanding of the plasmon-driven photocatalysis to the next level of depth and comprehensiveness relies critically on the development of new materials systems, approaches, and methodologies that transcend the disciplinary boundaries, which broadly embraces collaborative efforts among researchers in the plasmonics, spectroscopies, surface science, and computational chemistry communities.

Conflicts of interest

There are no conflicts of interest to declare.

Acknowledgements

The authors acknowledge the United States National Science Foundation (DMR-1253231 and OIA-1655740) and the University of South Carolina (Startup Funds, an ASPIRE-I Track I Award, and an ASPIRE-I Track IV Award) for funding support.

References

1 V. Biju, *Chem. Soc. Rev.*, 2014, **43**, 744–764.
2 M. A. Boles, D. Ling, T. Hyeon and D. V. Talapin, *Nat. Mater.*, 2016, **15**, 141–153.
3 H. Heinz, C. Pramanik, O. Heinz, Y. F. Ding, R. K. Mishra, D. Marchon, R. J. Flatt, I. Estrela-Lopis, J. Llop, S. Moya and R. F. Ziolo, *Surf. Sci. Rep.*, 2017, **72**, 1–58.
4 R. M. Choueiri, E. Galati, H. Therien-Aubin, A. Klinkova, E. M. Larin, A. Querejeta-Fernandez, L. L. Han, H. L. Xin, O. Gang, E. B. Zhulina, M. Rubinstein and E. Kumacheva, *Nature*, 2016, **538**, 79–83.
5 G. A. DeVries, M. Brunnbauer, Y. Hu, A. M. Jackson, B. Long, B. T. Neltner, O. Uzun, B. H. Wunsch and F. Stellacci, *Science*, 2007, **315**, 358–361.
6 Y. Kim, R. J. Macfarlane, M. R. Jones and C. A. Mirkin, *Science*, 2016, **351**, 579–582.
7 M. V. Kovalenko, M. Scheele and D. V. Talapin, *Science*, 2009, **324**, 1417–1420.
8 J. Owen, *Science*, 2015, **347**, 615–616.
9 D. V. Talapin, J. S. Lee, M. V. Kovalenko and E. V. Shevchenko, *Chem. Rev.*, 2010, **110**, 389–458.
10 D. Zherebetskyy, M. Scheele, Y. J. Zhang, N. Bronstein, C. Thompson, D. Britt, M. Salmeron, P. Alivisatos and L. W. Wang, *Science*, 2014, **344**, 1380–1384.
11 A. M. Jackson, J. W. Myerson and F. Stellacci, *Nat. Mater.*, 2004, **3**, 330–336.
12 D. W. Wang, R. J. Nap, I. Lagzi, B. Kowalczyk, S. B. Han, B. A. Grzybowski and I. Szleifer, *J. Am. Chem. Soc.*, 2011, **133**, 2192–2197.
13 A. Zaki, N. Dave and J. W. Liu, *J. Am. Chem. Soc.*, 2012, **134**, 35–38.
14 Y. B. Zheng, J. L. Payton, T. B. Song, B. K. Pathem, Y. X. Zhao, H. Ma, Y. Yang, L. Jensen, A. K. Y. Jen and P. S. Weiss, *Nano Lett.*, 2012, **12**, 5362–5368.
15 D. A. Walker, E. K. Leitsch, R. J. Nap, I. Szleifer and B. A. Grzybowski, *Nat. Nanotechnol.*, 2013, **8**, 676–681.
16 E. Villarreal, G. F. G. Li, Q. F. Zhang, X. Q. Fu and H. Wang, *Nano Lett.*, 2017, **17**, 4443–4452.
17 E. C. Dreaden, A. M. Alkilany, X. H. Huang, C. J. Murphy and M. A. El-Sayed, *Chem. Soc. Rev.*, 2012, **41**, 2740–2779.
18 R. C. Jin, C. J. Zeng, M. Zhou and Y. X. Chen, *Chem. Rev.*, 2016, **116**, 10346–10413.
19 C. J. Murphy, L. B. Thompson, A. M. Alkilany, P. N. Sisco, S. P. Boulos, S. T. Sivapalan, J. A. Yang, D. J. Chernak and J. Y. Huang, *J. Phys. Chem. Lett.*, 2010, **1**, 2867–2875.
20 I. Kherbouche, Y. Luo, N. Felidj and C. Mangeney, *Chem. Mater.*, 2020, **32**, 5442–5454.
21 A. Gelle, T. Jin, L. de la Garza, G. D. Price, L. V. Besteiro and A. Moores, *Chem. Rev.*, 2020, **120**, 986–1041.
22 Z. L. Zhang, C. Y. Zhang, H. R. Zheng and H. X. Xu, *Acc. Chem. Res.*, 2019, **52**, 2506–2515.
23 H. Wang, D. W. Brandl, P. Nordlander and N. J. Halas, *Acc. Chem. Res.*, 2007, **40**, 53–62.
24 S. Eustis and M. A. El-Sayed, *Chem. Soc. Rev.*, 2006, **35**, 209–217.
25 E. Hutter and J. H. Fendler, *Adv. Mater.*, 2004, **16**, 1685–1706.
26 S. Link and M. A. El-Sayed, *J. Phys. Chem. B*, 1999, **103**, 8410–8426.
27 K. A. Willets and R. P. Van Duyne, *Annu. Rev. Phys. Chem.*, 2007, **58**, 267–297.
28 J. N. Anker, W. P. Hall, O. Lyandres, N. C. Shah, J. Zhao and R. P. Van Duyne, *Nat. Mater.*, 2008, **7**, 442–453.
29 N. J. Halas, S. Lal, W. S. Chang, S. Link and P. Nordlander, *Chem. Rev.*, 2011, **111**, 3913–3961.
30 L. Novotny and N. van Hulst, *Nat. Photonics*, 2011, **5**, 83–90.
31 M. L. Brongersma, N. J. Halas and P. Nordlander, *Nat. Nanotechnol.*, 2015, **10**, 25–34.
32 Y. C. Zhang, S. He, W. X. Guo, Y. Hu, J. W. Huang, J. R. Mulcahy and W. D. Wei, *Chem. Rev.*, 2018, **118**, 2927–2954.

33 P. Christopher and M. Moskovits, in *Annu. Rev. Phys. Chem.*, ed. M. A. Johnson and T. J. Martinez, 2017, vol. 68, pp. 379–398.
34 M. J. Kale, T. Avanesian and P. Christopher, *ACS Catal.*, 2014, **4**, 116–128.
35 P. Christopher, H. L. Xin and S. Linic, *Nat. Chem.*, 2011, **3**, 467–472.
36 S. Linic, U. Aslam, C. Boerigter and M. Morabito, *Nat. Mater.*, 2015, **14**, 567–576.
37 S. Linic, P. Christopher and D. B. Ingram, *Nat. Mater.*, 2011, **10**, 911–921.
38 S. Linic, P. Christopher, H. L. Xin and A. Marimuthu, *Acc. Chem. Res.*, 2013, **46**, 1890–1899.
39 S. Mukherjee, F. Libisch, N. Large, O. Neumann, L. V. Brown, J. Cheng, J. B. Lassiter, E. A. Carter, P. Nordlander and N. J. Halas, *Nano Lett.*, 2013, **13**, 240–247.
40 J. Lee, S. Mubeen, X. L. Ji, G. D. Stucky and M. Moskovits, *Nano Lett.*, 2012, **12**, 5014–5019.
41 C. Zhan, M. Moskovits and Z. Q. Tian, *Matter*, 2020, **3**, 42–56.
42 Y. Zhang, E. Villarreal, G. G. Li, W. Wang and H. Wang, *J. Phys. Chem. Lett.*, 2020, **11**, 9321–9328.
43 Y. Fang, N. H. Seong and D. D. Dlott, *Science*, 2008, **321**, 388–392.
44 J. F. Li, Y. F. Huang, Y. Ding, Z. L. Yang, S. B. Li, X. S. Zhou, F. R. Fan, W. Zhang, Z. Y. Zhou, D. Y. Wu, B. Ren, Z. L. Wang and Z. Q. Tian, *Nature*, 2010, **464**, 392–395.
45 A. Campion and P. Kambhampati, *Chem. Soc. Rev.*, 1998, **27**, 241–250.
46 S. Y. Ding, J. Yi, J. F. Li, B. Ren, D. Y. Wu, R. Panneerselvam and Z. Q. Tian, *Nat. Rev. Mater.*, 2016, **1**, 16021.
47 J. Kneipp, H. Kneipp and K. Kneipp, *Chem. Soc. Rev.*, 2008, **37**, 1052–1060.
48 K. Kneipp, H. Kneipp, I. Itzkan, R. R. Dasari and M. S. Feld, *Chem. Rev.*, 1999, **99**, 2957–2976.
49 S. Schlucker, *Angew. Chem., Int. Ed.*, 2014, **53**, 4756–4795.
50 S. Y. Ding, E. M. You, Z. Q. Tian and M. Moskovits, *Chem. Soc. Rev.*, 2017, **46**, 4042–4076.
51 F. J. GarciaVidal and J. B. Pendry, *Phys. Rev. Lett.*, 1996, **77**, 1163–1166.
52 M. Moskovits, *J. Raman Spectrosc.*, 2005, **36**, 485–496.
53 J. Langer, D. J. de Aberasturi, J. Aizpurua, R. A. Alvarez-Puebla, B. Auguie, J. J. Baumberg, G. C. Bazan, S. E. J. Bell, A. Boisen, A. G. Brolo, J. Choo, D. Cialla-May, V. Deckert, L. Fabris, K. Faulds, F. J. G. de Abajo, R. Goodacre, D. Graham, A. J. Haes, C. L. Haynes, C. Huck, T. Itoh, M. Ka, J. Kneipp, N. A. Kotov, H. Kuang, E. C. Le Ru, H. K. Lee, J. F. Li, X. Y. Ling, S. A. Maier, T. Mayerhofer, M. Moskovits, K. Murakoshi, J. M. Nam, S. Nie, Y. Ozaki, I. Pastoriza-Santos, J. Perez-Juste, J. Popp, A. Pucci, S. Reich, B. Ren, G. C. Schatz, T. Shegai, S. Schlucker, L. L. Tay, K. G. Thomas, Z. Q. Tian, R. P. Van Duyne, T. Vo-Dinh, Y. Wang, K. A. Willets, C. Xu, H. Xu, Y. Xu, Y. S. Yamamoto, B. Zhao and L. M. Liz-Marzan, *ACS Nano*, 2020, **14**, 28–117.
54 A. Otto, *Top. Appl. Phys.*, 1984, **54**, 289–418.
55 A. Otto, *J. Raman Spectrosc.*, 2005, **36**, 497–509.
56 M. Moskovits, *Rev. Mod. Phys.*, 1985, **57**, 783–826.
57 J. P. Camden, J. A. Dieringer, Y. M. Wang, D. J. Masiello, L. D. Marks, G. C. Schatz and R. P. Van Duyne, *J. Am. Chem. Soc.*, 2008, **130**, 12616–12617.
58 K. Kneipp, Y. Wang, H. Kneipp, L. T. Perelman, I. Itzkan, R. Dasari and M. S. Feld, *Phys. Rev. Lett.*, 1997, **78**, 1667–1670.
59 D. K. Lim, K. S. Jeon, H. M. Kim, J. M. Nam and Y. D. Suh, *Nat. Mater.*, 2010, **9**, 60–67.
60 X. M. Qian and S. M. Nie, *Chem. Soc. Rev.*, 2008, **37**, 912–920.
61 H. X. Xu, E. J. Bjerneld, M. Kall and L. Borjesson, *Phys. Rev. Lett.*, 1999, **83**, 4357–4360.
62 S. M. Nie and S. R. Emory, *Science*, 1997, **275**, 1102–1106.
63 B. Sharma, R. R. Frontiera, A. I. Henry, E. Ringe and R. P. Van Duyne, *Mater. Today*, 2012, **15**, 16–25.
64 S. Shi and D. Qin, *Angew. Chem., Int. Ed.*, 2020, **59**, 3782–3792.
65 H. Wang, Q. F. Zhang, E. Villarreal, H. Jing and K. Chen, *Journal of the South Carolina Academy of Science*, 2020, **18**, 4–11.
66 K. N. Heck, B. G. Janesko, G. E. Scuseria, N. J. Halas and M. S. Wong, *J. Am. Chem. Soc.*, 2008, **130**, 16592–16600.
67 V. Joseph, C. Engelbrekt, J. D. Zhang, U. Gernert, J. Ulstrup and J. Kneipp, *Angew. Chem., Int. Ed.*, 2012, **51**, 7592–7596.
68 J. F. Huang, Y. H. Zhu, M. Lin, Q. X. Wang, L. Zhao, Y. Yang, K. X. Yao and Y. Han, *J. Am. Chem. Soc.*, 2013, **135**, 8552–8561.
69 H. Jing, Q. F. Zhang, N. Large, C. M. Yu, D. A. Blom, P. Nordlander and H. Wang, *Nano Lett.*, 2014, **14**, 3674–3682.
70 W. Xie, C. Herrmann, K. Kompe, M. Haase and S. Schlucker, *J. Am. Chem. Soc.*, 2011, **133**, 19302–19305.
71 Q. F. Zhang, D. A. Blom and H. Wang, *Chem. Mater.*, 2014, **26**, 5131–5142.
72 Q. F. Zhang, L. L. Han, H. Jing, D. A. Blom, Y. Lin, H. L. L. Xing and H. Wang, *ACS Nano*, 2016, **10**, 2960–2974.
73 Q. F. Zhang and H. Wang, *ACS Catal.*, 2014, **4**, 4027–4033.
74 Q. F. Zhang, Y. D. Zhou, E. Villarreal, Y. Lin, S. L. Zou and H. Wang, *Nano Lett.*, 2015, **15**, 4161–4169.
75 J. Ahn, S. Shi, B. Vannatter and D. Qin, *J. Phys. Chem. C*, 2019, **123**, 21571–21580.
76 Y. L. Li, Y. F. Hu, F. X. Shi, H. X. Li, W. Xie and J. Chen, *Angew. Chem., Int. Ed.*, 2019, **58**, 9049–9053.
77 W. Xie, R. Grzeschik and S. Schlucker, *Angew. Chem., Int. Ed.*, 2016, **55**, 13729–13733.
78 K. F. Zhang, L. Yang, Y. F. Hu, C. H. Fan, Y. R. Zhao, L. Bai, Y. L. Li, F. X. Shi, J. Liu and W. Xie, *Angew. Chem., Int. Ed.*, 2020, **59**, 18003–18009.
79 Y. R. Zhao, L. L. Du, H. X. Li, W. Xie and J. Chen, *J. Phys. Chem. Lett.*, 2019, **10**, 1286–1291.
80 W. Xie, B. Walkenfort and S. Schlucker, *J. Am. Chem. Soc.*, 2013, **135**, 1657–1660.
81 B. M. DeVetter, P. Mukherjee, C. J. Murphy and R. Bhargava, *Nanoscale*, 2015, **7**, 8766–8775.
82 E. Kazuma and Y. Kim, *Angew. Chem., Int. Ed.*, 2019, **58**, 4800–4808.
83 J. Gargiulo, R. Berte, Y. Li, S. A. Maier and E. Cortes, *Acc. Chem. Res.*, 2019, **52**, 2525–2535.

84 J. B. Khurgin, *Faraday Discuss.*, 2019, **214**, 35–58.
85 G. Baffou, P. Bon, J. Savatier, J. Polleux, M. Zhu, M. Merlin, H. Rigneault and S. Monneret, *ACS Nano*, 2012, **6**, 2452–2458.
86 G. Baffou, I. Bordacchini, A. Baldi and R. Quidant, *Light: Sci. Appl.*, 2020, **9**, 108.
87 G. Baffou, H. Rigneault, D. Marguet and L. Jullien, *Nat. Methods*, 2014, **11**, 899–901.
88 Y. Dubi, I. W. Un and Y. Sivan, *Chem. Sci.*, 2020, **11**, 5017–5027.
89 Y. Sivan, J. Baraban, I. W. Un and Y. Dubi, *Science*, 2019, **364**, eaaw9367.
90 Y. Sivan, I. W. Un and Y. Dubi, *Faraday Discuss.*, 2019, **214**, 215–233.
91 P. K. Jain, *J. Phys. Chem. C*, 2019, **123**, 24347–24351.
92 S. Rej, L. Mascaretti, E. Y. Santiago, O. Tomanec, S. Kment, Z. M. Wang, R. Zboril, P. Fornasiero, A. O. Govorov and A. Naldoni, *ACS Catal.*, 2020, **10**, 5261–5271.
93 C. Zhan, B. W. Liu, Y. F. Huang, S. Hu, B. Ren, M. Moskovits and Z. Q. Tian, *Nat. Commun.*, 2019, **10**, 2671.
94 X. Q. Li, H. O. Everitt and J. Liu, *Nano Res.*, 2020, **13**, 1268–1280.
95 X. Zhang, X. Q. Li, M. E. Reish, D. Zhang, N. Q. Su, Y. Gutierrez, F. Moreno, W. T. Yang, H. O. Everitt and J. Liu, *Nano Lett.*, 2018, **18**, 1714–1723.
96 Y. Dubi and Y. Sivan, *Light: Sci. Appl.*, 2019, **8**, 89.
97 L. A. Zhou, D. F. Swearer, C. Zhang, H. Robatjazi, H. Q. Zhao, L. Henderson, L. L. Dong, P. Christopher, E. A. Carter, P. Nordlander and N. J. Halas, *Science*, 2018, **362**, 69–72.
98 B. Seemala, A. J. Therrien, M. H. Lou, K. Li, J. P. Finzel, J. Qi, P. Nordlander and P. Christopher, *ACS Energy Lett.*, 2019, **4**, 1803–1809.
99 K. Wu, J. Chen, J. R. McBride and T. Lian, *Science*, 2015, **349**, 632–635.
100 B. Foerster, V. A. Spata, E. A. Carter, C. Sonnichsen and S. Link, *Sci. Adv.*, 2019, **5**, eaav0704.
101 A. M. Glass, P. F. Liao, J. G. Bergman and D. H. Olson, *Opt. Lett.*, 1980, **5**, 368–370.
102 T. E. Tesema, H. Kookhaee and T. G. Habteyes, *J. Phys. Chem. Lett.*, 2020, **11**, 3507–3514.
103 Y. F. Huang, H. P. Zhu, G. K. Liu, D. Y. Wu, B. Ren and Z. Q. Tian, *J. Am. Chem. Soc.*, 2010, **132**, 9244–9246.
104 M. T. Sun and H. X. Xu, *Small*, 2012, **8**, 2777–2786.
105 X. J. Chen, G. Cabello, D. Y. Wu and Z. Q. Tian, *J. Photochem. Photobiol., C*, 2014, **21**, 54–80.
106 C. Zhan, X. J. Chen, Y. F. Huang, D. Y. Wu and Z. Q. Tian, *Acc. Chem. Res.*, 2019, **52**, 2784–2792.
107 L. B. Zhao, M. Zhang, Y. F. Huang, C. T. Williams, D. Y. Wu, B. Ren and Z. Q. Tian, *J. Phys. Chem. Lett.*, 2014, **5**, 1259–1266.
108 M. Osawa, N. Matsuda, K. Yoshii and I. Uchida, *J. Phys. Chem.*, 1994, **98**, 12702–12707.
109 X. M. Yang, D. A. Tryk, K. Ajito, K. Hashimoto and A. Fujishima, *Langmuir*, 1996, **12**, 5525–5527.
110 X. M. Yang, D. A. Tryk, K. Hashimoto and A. Fujishima, *J. Raman Spectrosc.*, 1998, **29**, 725–732.
111 P. Xu, L. L. Kang, N. H. Mack, K. S. Schanze, X. J. Han and H. L. Wang, *Sci. Rep.*, 2013, **3**, 2997.
112 Y. R. Fang, Y. Z. Li, H. X. Xu and M. T. Sun, *Langmuir*, 2010, **26**, 7737–7746.
113 M. T. Sun, Y. Z. Huang, L. X. Xia, X. W. Chen and H. X. Xu, *J. Phys. Chem. C*, 2011, **115**, 9629–9636.
114 N. Takeyasu, R. Kagawa, K. Sakata and T. Kaneta, *J. Phys. Chem. C*, 2016, **120**, 12163–12169.
115 Y. F. Huang, M. Zhang, L. B. Zhao, J. M. Feng, D. Y. Wu, B. Ren and Z. Q. Tian, *Angew. Chem., Int. Ed.*, 2014, **53**, 2353–2357.
116 Y. Z. Huang, Y. R. Fang, Z. L. Yang and M. T. Sun, *J. Phys. Chem. C*, 2010, **114**, 18263–18269.
117 D. Y. Wu, X. M. Liu, Y. F. Huang, B. Ren, X. Xu and Z. Q. Tian, *J. Phys. Chem. C*, 2009, **113**, 18212–18222.
118 V. Canpean, M. Iosin and S. Astilean, *Chem. Phys. Lett.*, 2010, **500**, 277–282.
119 Q. Zhang and H. Wang, *J. Phys. Chem. C*, 2018, **122**, 5686–5697.
120 X. Gu, H. Wang and J. P. Camden, *Chem. Sci.*, 2017, **8**, 5902–5908.
121 J. Y. Chu, P. Miao, X. J. Han, Y. C. Du, X. J. Wang, B. Song and P. Xu, *ChemCatChem*, 2016, **8**, 1819–1824.
122 X. F. Yan, L. Z. Wang, X. J. Tan, B. Z. Tian and J. L. Zhang, *Sci. Rep.*, 2016, **6**, 30193.
123 B. Kafle, M. Poveda and T. G. Habteyes, *J. Phys. Chem. Lett.*, 2017, **8**, 890–894.
124 B. Dong, Y. R. Fang, X. W. Chen, H. X. Xu and M. T. Sun, *Langmuir*, 2011, **27**, 10677–10682.
125 L. L. Kang, P. Xu, B. Zhang, H. H. Tsai, X. J. Han and H. L. Wang, *Chem. Commun.*, 2013, **49**, 3389–3391.
126 B. Dong, Y. R. Fang, L. X. Xia, H. X. Xu and M. T. Sun, *J. Raman Spectrosc.*, 2011, **42**, 1205–1206.
127 H. K. Choi, K. S. Lee, H. H. Shin and Z. H. Kim, *J. Phys. Chem. Lett.*, 2016, **7**, 4099–4104.
128 L.-B. Zhao, Y.-F. Huang, X.-M. Liu, J. R. Anema, D.-Y. Wu, B. Ren and Z.-Q. Tian, *Phys. Chem. Chem. Phys.*, 2012, **14**, 12919–12929.
129 E. M. van Schrojenstein Lantman, T. Deckert-Gaudig, A. J. Mank, V. Deckert and B. M. Weckhuysen, *Nat. Nanotechnol.*, 2012, **7**, 583–586.
130 C. F. Wang, B. T. O'Callahan, D. Kurouski, A. Krayev and P. Z. El-Khoury, *J. Phys. Chem. Lett.*, 2020, **11**, 3809–3814.
131 R. Schürmann, T. F. M. Luxford, I. S. Vinklarek, J. Kocisek, M. Zawadzki and I. Bald, *J. Chem. Phys.*, 2020, **153**, 104303.
132 W. Xie and S. Schlücker, *Nat. Commun.*, 2015, **6**, 7570.
133 H. K. Choi, W. H. Park, C. G. Park, H. H. Shin, K. S. Lee and Z. H. Kim, *J. Am. Chem. Soc.*, 2016, **138**, 4673–4684.
134 J. L. Brooks and R. R. Frontiera, *J. Phys. Chem. C*, 2016, **120**, 20869–20876.
135 R. M. Sarhan, W. Koopman, J. Pudell, F. Stete, M. Rossle, M. Herzog, C. N. Z. Schmitt, F. Liebig, J. Koetz and M. Bargheer, *J. Phys. Chem. C*, 2019, **123**, 9352–9357.
136 W. Koopman, R. M. Sarhan, F. Stete, C. N. Z. Schmitt and M. Bargheer, *Nanoscale*, 2020, **12**, 24411–24418.

137 Q. F. Zhang, Y. D. Zhou, X. Q. Fu, E. Villarreal, L. C. Sun, S. L. Zou and H. Wang, *J. Phys. Chem. C*, 2019, **123**, 26695–26704.

138 L. L. Kang, X. J. Han, J. Y. Chu, J. Xiong, X. He, H. L. Wang and P. Xu, *ChemCatChem*, 2015, **7**, 1004–1010.

139 J. J. Sun, H. S. Su, H. L. Yue, S. C. Huang, T. X. Huang, S. Hu, M. M. Sartin, J. Cheng and B. Ren, *J. Phys. Chem. Lett.*, 2019, **10**, 2306–2312.

140 E. L. Keller and R. R. Frontiera, *ACS Nano*, 2018, **12**, 5848–5855.

141 H. H. Richardson, M. T. Carlson, P. J. Tandler, P. Hernandez and A. O. Govorov, *Nano Lett.*, 2009, **9**, 1139–1146.

142 G. Baffou, P. Berto, E. B. Urena, R. Quidant, S. Monneret, J. Polleux and H. Rigneault, *ACS Nano*, 2013, **7**, 6478–6488.

143 G. Baffou and H. Rigneault, *Phys. Rev. B: Condens. Matter Mater. Phys.*, 2011, **84**, 035415.

144 R. Kamarudheen, G. W. Castellanos, L. P. J. Kamp, H. J. H. Clercx and A. Baldi, *ACS Nano*, 2018, **12**, 8447–8455.

145 I. W. Un and Y. Sivan, *Nanoscale*, 2020, **12**, 17821–17832.

146 X. H. Xu, A. Dutta, J. Khurgin, A. L. Wei, V. M. Shalaev and A. Boltasseva, *Laser Photonics Rev.*, 2020, **14**, 1900376.

147 R. M. Sarhan, W. Koopman, R. Schuetz, T. Schmid, F. Liebig, J. Koetz and M. Bargheer, *Sci. Rep.*, 2019, **9**, 3060.

148 A. A. Golubev, B. N. Khlebtsov, R. D. Rodriguez, Y. Chen and D. R. T. Zahn, *J. Phys. Chem. C*, 2018, **122**, 5657–5663.

149 A. Streitwieser, Jr. and C. H. Heathcock, *Introduction to Organic Chemistry*, Macmillan Publishing Company, New York, 1989.

150 L. J. Goossen, N. Rodriguez, B. Melzer, C. Linder, G. J. Deng and L. M. Levy, *J. Am. Chem. Soc.*, 2007, **129**, 4824–4833.

151 L. J. Goossen, W. R. Thiel, N. Rodriguez, C. Linder and B. Melzer, *Adv. Synth. Catal.*, 2007, **349**, 2241–2246.

152 A. Michota and J. Bukowska, *J. Raman Spectrosc.*, 2003, **34**, 21–25.

153 Y. Wang, W. Ji, H. M. Sui, Y. Kitahama, W. D. Ruan, Y. Ozaki and B. Zhao, *J. Phys. Chem. C*, 2014, **118**, 10191–10197.

154 Y. Zong, Q. H. Guo, M. M. Xu, Y. X. Yuan, R. N. Gu and J. L. Yao, *RSC Adv.*, 2014, **4**, 31810–31816.

155 H. Huh, H. D. Trinh, D. Lee and S. Yoon, *ACS Appl. Mater. Interfaces*, 2019, **11**, 24715–24724.

156 L. T. M. Huynh, H. D. Trinh, S. Lee and S. Yoon, *Nanoscale*, 2020, **12**, 24062–24069.

157 Z. L. Zhang, T. Deckert-Gaudig, P. Singh and V. Deckert, *Chem. Commun.*, 2015, **51**, 3069–3072.

158 G. Smith, J. S. Girardon, J. F. Paul and E. Berrier, *Phys. Chem. Chem. Phys.*, 2016, **18**, 19567–19573.

159 T. E. Tesema, C. Annesley and T. G. Habteyes, *J. Phys. Chem. C*, 2018, **122**, 19831–19841.

160 T. E. Tesema, B. Kafle, M. G. Tadesse and T. G. Habteyes, *J. Phys. Chem. C*, 2017, **121**, 7421–7428.

161 T. E. Tesema, B. Kafle and T. G. Habteyes, *J. Phys. Chem. C*, 2019, **123**, 8469–8483.

162 E. Kazuma, J. Jung, H. Ueba, M. Trenary and Y. Kim, *Science*, 2018, **360**, 521–525.

163 C. Boerigter, R. Campana, M. Morabito and S. Linic, *Nat. Commun.*, 2016, **7**, 10545.

164 C. Boerigter, U. Aslam and S. Linic, *ACS Nano*, 2016, **10**, 6108–6115.

165 M. R. Beversluis, A. Bouhelier and L. Novotny, *Phys. Rev. B: Condens. Matter Mater. Phys.*, 2003, **68**, 115433.

166 T. V. Shahbazyan, *Nano Lett.*, 2013, **13**, 194–198.

167 O. P. Varnavski, T. Goodson, M. B. Mohamed and M. A. El-Sayed, *Phys. Rev. B: Condens. Matter Mater. Phys.*, 2005, **72**, 235405.

168 J. Huang, W. Wang, C. J. Murphy and D. G. Cahill, *Proc. Natl. Acad. Sci. U. S. A.*, 2014, **111**, 906–911.

169 J. T. Hugall and J. J. Baumberg, *Nano Lett.*, 2015, **15**, 2600–2604.

170 Y.-Y. Cai, E. Sung, R. Zhang, L. J. Tauzin, J. G. Liu, B. Ostovar, Y. Zhang, W.-S. Chang, P. Nordlander and S. Link, *Nano Lett.*, 2019, **19**, 1067–1073.

171 X. Xie and D. G. Cahill, *Appl. Phys. Lett.*, 2016, **109**, 183104.

172 M. Virk, K. Xiong, M. Svedendahl, M. Kall and A. B. Dahlin, *Nano Lett.*, 2014, **14**, 3544–3549.

173 D. Andren, L. Shao, N. O. Lank, S. S. Acimovic, P. Johansson and M. Kall, *ACS Nano*, 2017, **11**, 10053–10061.

174 P. Singh and V. Deckert, *Chem. Commun.*, 2014, **50**, 11204–11207.

175 B. B. Zhou, S. F. Li, X. H. Tang, P. Li, X. M. Cao, B. R. Yu, L. B. Yang and J. H. Liu, *Nanoscale*, 2017, **9**, 12307–12310.

176 R. Schürmann and I. Bald, *Nanoscale*, 2017, **9**, 1951–1955.

177 S. Chaunchaiyakul, A. Setiadi, P. Krukowski, F. C. I. Catalan, M. Akai-Kasaya, A. Saito, N. Hayazawa, Y. Kim, H. Osuga and Y. Kuwahara, *J. Phys. Chem. C*, 2017, **121**, 18162–18168.

178 E. Miliutina, O. Guselnikova, N. S. Soldatova, P. Bainova, R. Elashnikov, P. Fitl, T. Kurten, M. S. Yusubov, V. Svorcik, R. R. Valiev, M. M. Chehimi, O. Lyutakov and P. S. Postnikov, *J. Phys. Chem. Lett.*, 2020, **11**, 5770–5776.

179 J. L. Brooks, D. V. Chulhai, Z. W. Yu, J. D. Goodpaster and R. R. Frontiera, *J. Phys. Chem. C*, 2019, **123**, 29306–29313.

180 J. Szczerbinski, L. Gyr, J. Kaeslin and R. Zenobi, *Nano Lett.*, 2018, **18**, 6740–6749.

181 W. Geyer, V. Stadler, W. Eck, M. Zharnikov, A. Gölzhäuser and M. Grunze, *Appl. Phys. Lett.*, 1999, **75**, 2401–2403.

182 M. Zharnikov, W. Geyer, A. Gölzhäuser, S. Frey and M. Grunze, *Phys. Chem. Chem. Phys.*, 1999, **1**, 3163–3171.

183 F. Wang, C. H. Li, H. J. Chen, R. B. Jiang, L. D. Sun, Q. Li, J. F. Wang, J. C. Yu and C. H. Yan, *J. Am. Chem. Soc.*, 2013, **135**, 5588–5601.

184 A. O. Govorov, H. Zhang, H. V. Demir and Y. K. Gun'ko, *Nano Today*, 2014, **9**, 85–101.

185 J. Zhao, S. C. Nguyen, R. Ye, B. H. Ye, H. Weller, G. A. Somorjai, A. P. Alivisatos and F. D. Toste, *ACS Cent. Sci.*, 2017, **3**, 482–488.

186 S. Roy, S. Roy, A. Rao, G. Devatha and P. P. Pillai, *Chem. Mater.*, 2018, **30**, 8415–8419.

187 Y. Kim, D. D. Torres and P. K. Jain, *Nano Lett.*, 2016, **16**, 3399–3407.

188 X. Q. Fu, G. G. Li, E. Villarreal and H. Wang, *Nanoscale*, 2019, **11**, 7324–7334.
189 Z. L. Mao, R. Espinoza, A. Garcia, A. Enwright, H. Vang and S. C. Nguyen, *ACS Nano*, 2020, **14**, 7038–7045.
190 X. P. Zhang, C. Y. Huang, M. Wang, P. Huang, X. K. He and Z. Y. Wei, *Sci. Rep.*, 2018, **8**, 10499.
191 G. V. Naik, V. M. Shalaev and A. Boltasseva, *Adv. Mater.*, 2013, **25**, 3264–3294.
192 Y. Gutiérrez, A. S. Brown, F. Moreno and M. Losurdo, *J. Appl. Phys.*, 2020, **128**, 080901.
193 A. Agrawal, S. H. Cho, O. Zandi, S. Ghosh, R. W. Johns and D. J. Milliron, *Chem. Rev.*, 2018, **118**, 3121–3207.
194 M. W. Knight, N. S. King, L. F. Liu, H. O. Everitt, P. Nordlander and N. J. Halas, *ACS Nano*, 2014, **8**, 834–840.
195 M. W. Knight, L. F. Liu, Y. M. Wang, L. Brown, S. Mukherjee, N. S. King, H. O. Everitt, P. Nordlander and N. J. Halas, *Nano Lett.*, 2012, **12**, 6000–6004.
196 L. Zhou, C. Zhang, M. J. McClain, A. Manavacas, C. M. Krauter, S. Tian, F. Berg, H. O. Everitt, E. A. Carter, P. Nordlander and N. J. Halas, *Nano Lett.*, 2016, **16**, 1478–1484.
197 J. S. Biggins, S. Yazdi and E. Ringe, *Nano Lett.*, 2018, **18**, 3752–3758.
198 M. Q. Sun, X. Q. Fu, K. X. Chen and H. Wang, *ACS Appl. Mater. Interfaces*, 2020, **12**, 46146–46161.
199 X. Y. Gan, E. L. Keller, C. L. Warkentin, S. E. Crawford, R. R. Frontiera and J. E. Millstone, *Nano Lett.*, 2019, **19**, 2384–2388.
200 Y. Zhao, H. Pan, Y. Lou, X. Qiu, J. Zhu and C. Burda, *J. Am. Chem. Soc.*, 2009, **131**, 4253–4261.
201 J. M. Luther, P. K. Jain, T. Ewers and A. P. Alivisatos, *Nat. Mater.*, 2011, **10**, 361–366.
202 D. Dorfs, T. Härtling, K. Miszta, N. C. Bigall, M. R. Kim, A. Genovese, A. Falqui, M. Povia and L. Manna, *J. Am. Chem. Soc.*, 2011, **133**, 11175–11180.
203 S.-W. Hsu, K. On and A. R. Tao, *J. Am. Chem. Soc.*, 2011, **133**, 19072–19075.
204 I. Kriegel, J. Rodríguez-Fernández, A. Wisnet, H. Zhang, C. Waurisch, A. Eychmüller, A. Dubavik, A. O. Govorov and J. Feldmann, *ACS Nano*, 2013, **7**, 4367–4377.
205 Y. Xie, L. Carbone, C. Nobile, V. Grillo, S. D'Agostino, F. Della Sala, C. Giannini, D. Altamura, C. Oelsner, C. Kryschi and P. D. Cozzoli, *ACS Nano*, 2013, **7**, 7352–7369.
206 W. Li, R. Zamani, P. Rivera Gil, B. Pelaz, M. Ibáñez, D. Cadavid, A. Shavel, R. A. Alvarez-Puebla, W. J. Parak, J. Arbiol and A. Cabot, *J. Am. Chem. Soc.*, 2013, **135**, 7098–7101.
207 A. Agrawal, R. W. Johns and D. J. Milliron, *Annu. Rev. Mater. Res.*, 2017, **47**, 1–31.

